Homogenization Techniques Taking Account of Eddy Currents in Magnetic Field Analysis

September 2014

Lin Cheng

Department of Science and Advanced Technology

Graduate School of Science and Engineering

Saga University

Acknowledgements

My deepest gratitude goes first and foremost to Professor Kazuhiro Muramatsu, my supervisor, for his constant encouragement and guidance. He has walked me through all the stages of the writing of this thesis. Without his consistent and illuminating instruction, this thesis could not have reached its present form.

Second, I would like to express my heartfelt gratitude to Professor Eiji Takahashi, Professor Satoru Goto, and Doctor Hiroshi Dozono for their valuable comments and suggestions as the members of this dissertation committee.

Third, I am also indebted to the MONBUKAGAKUSHO (Ministry of Education, Culture, Sports, Science and Technology), Government of Japan, for their financial support during my study in Saga University.

Forth, I am also greatly indebted to Doctor Yanhui Gao, who have instructed and helped me a lot in the past three years.

Fifth, thank you for the friends in the lab: Mr. Hassan Ebrahimi，Dr. Shunya Odawara, and Mr. Kenji Ikenaga, who have helped me a lot in the past three years.

My last thanks would go to my beloved family for their loving considerations and great confidence in me all through these years. I also owe my sincere gratitude to my friends who gave me their help and time in listening to me and helping me work out my problems during the difficult course of the thesis.

TABLE OF CONTENTS

Chapter 1 Introduction

1.1 Research background

1.1.1 Motivation

Recently, the three dimensional (3D) magnetic field analysis with the finite element method (FEM) is widely used to develop high performance electric machines and magnetic devices. However, great efforts toward the finite element modeling and huge computation costs are required in the magnetic field analyses of complete models composed of distributed components, such as a laminated core [1], a building [2-3], Open-Type Magnetically Shielded Room (MSR) [4] etc. To overcome these problems, homogenization techniques [5-15], in which the complicatedly distributed materials are replaced with a homogeneous body, are discussed at this moment.

In my research, homogenization techniques of a laminated core and a model composed of distributed components, are required to develop high performance electric machines and magnetic devices.

1.1.2 Modeling of laminated core

In electric machines, laminated cores are commonly used in order to reduce the eddy current losses. In the finite element analysis of the magnetic field in such a machine, the laminated core is normally modeled by a solid one in order to save computation cost. In the ordinary method, the eddy current in the core is neglected because the eddy current loops in laminated cores are much different from those in solid cores. However, it seems that the eddy current in the steel plate used for

laminating sometimes should not be neglected, such as in a machine with an inverter power supply in which the voltage has harmonic components.

In the analysis of a magnetic shielding with thin magnetic conductive layers carrying eddy currents, it has been already proposed that the magnetic field inside a layer is evaluated analytically [5], [6]. Then, it has been applied to the linear magnetic field analysis of the laminated core [7]. In that analysis, the laminated core is modeled by a solid one with anisotropic permeability and conductivity, and the permeability is determined by the analytical solution of the magnetic field inside the steel plate carrying the eddy current. Next, the method is expanded to nonlinear analysis by using the one-dimensional (1D) finite-element eddy current analysis instead of the analytical solution [8]. The Newton–Raphson method is applied to nonlinear iteration, and the step-by-step method is used for time iteration. The proposed method can obtain accurate average values of the flux and eddy current densities except for near the sides of cores, and the accurate eddy current losses, within the applicable CPU time. Moreover, the proposed homogenization technique is extended into the loss calculation [9]. In this loss calculation, the hysteresis loss in the laminated core is calculated considering the skin effect of the flux in steel plates and the eddy current loss in the steel plate can be directly calculated. This proposed method is applied to the loss calculation in a reactor connected to inverter power supply. The configurations of the core and the plate are improved by the loss distribution obtained from the proposed method. The iron loss can be reduced by half due to improvements in the experiment. However, the proposed technique cannot be applied to motor cores because the rotational flux cannot be taken into account by

using the 1D sub-analysis.

1.1.3 Modeling of models composed of distributed components

For example, to calculate the magnetic disturbance due to a building by using the magnetic field analysis with the FEM, great efforts toward modelling complicatedly distributed magnetic materials in buildings are required [2-3]. Moreover, huge memory and CPU time are also required due to the large number of elements. To overcome these problems, homogenization techniques [16-21], in which the complicatedly distributed materials are replaced with a homogeneous body, have already been proposed. In several techniques, the technique [19] based on the energy conservation seems to be attractive because the complicated shape and the nonlinearity can be easily considered. In this technique, the equivalent permeability of the homogeneous body is determined so that the energy is equal to that of the real model. Then, the homogenization technique is applied to the magnetic field analyses of a building and an open type of MSR [20]. It is shown that the homogenization technique should be applied to not only the region of the magnetic materials but also the air region surrounding them. Moreover, even if the homogenization technique is applied, similar results with the real model can be obtained by the reproduction. Moreover, an open-type MSR composed of magnetic cylinders for a magnetic resonance imaging (MRI) of 3T designed by the homogenization technique is built in a hospital and the effectiveness of homogenization techniques is verified [21]. However, the homogenization technique for a periodic conductive components taking account of eddy currents seems not established. This is because a 2D or 3D

eddy current analysis of the cell model is required to determine the effective permeability, moreover, the eddy current distributions are affected by insulation and conduction between conductive components.

1.2 Research purpose

1.2.1 Modeling of laminated core

In my research, the 1D eddy current analysis of one steel plate (sub-analysis) in the proposed homogenization technique is expanded to a 3D sub-analysis which can take account of the direction of the flux density, in the linear magnetic field analysis for simplicity. To investigate the effectiveness of the developed homogenization technique with the 3D sub-analysis, the proposed method is applied to a simple laminated core model under the rotational flux. The flux distribution, the eddy current distribution, and the eddy current loss obtained from using the proposed method are compared with those of the ordinary homogeneous solid core model with 1D steel plate model and the real laminated core model.

1.2.2 Modeling of models composed of distributed components

In my research, the homogenization techniques for periodic conductive and non-magnetic components are investigated using models of open-type electromagnetic shielding walls piled using square cylinders with and without gaps in linear ac steady-state eddy current problems. Two homogenization techniques are examined in both models. One is the technique homogenized by using a magnetic body with effective anisotropic complex permeability and without eddy currents.

This technique is based on that for the homogenization of laminated core. The other is the technique homogenized by using a non-magnetic conductive body with modified anisotropic conductivity. To clarify the suitable technique for each model with or without gaps, the shielding effects obtained using both homogenization techniques are compared with those obtained using the real models. Moreover, the methods for determining effective permeability and modified conductivity in both techniques are proposed and verified.

1.3 Organization of Thesis

In Chapter 1, the research background of this thesis is presented with an important viewpoint that the homogeneous techniques is important for modeling of laminated cores and models composed of distributed components.

Chapter 2 expresses the method of 3D eddy current analysis. First, the fundamental equations are introduced. Then, the discretization is carried out by FEM.

Chapter 3 expresses the homogenization technique of laminated cores under rotational fluxes. The homogenization technique with 3D sub-analysis is proposed. The proposed method is verified a simple laminated core model under the rotational flux.

Chapter 4 expresses the homogenization techniques of models composed of distributed components with and without gaps in linear ac steady-state eddy current problems. Two techniques using magnetic and conductive bodies are investigated.

Both techniques are applied to two models, in which each component is insulated and connected, and the results are verified.

Chapter 5 is the conclusion and recommendation for future work.

Chapter 2 Methods of 3D Eddy Current Analysis

2.1 Fundamental Equations

A. Maxwell equations [22-23]

The electromagnetic field follows the four Maxwell equations in differential form as follows:

$$\mathrm{rot}\,\boldsymbol{H} = \boldsymbol{J} + \frac{\partial \boldsymbol{D}}{\partial t} \tag{2-1}$$

$$\mathrm{rot}\,\boldsymbol{E} = -\frac{\partial \boldsymbol{B}}{\partial t} \tag{2-2}$$

$$\mathrm{div}\boldsymbol{D} = \rho \tag{2-3}$$

$$\mathrm{div}\boldsymbol{B} = 0 \tag{2-4}$$

where $\boldsymbol{B}$, $\boldsymbol{H}$, $\boldsymbol{J}$, $\boldsymbol{D}$, $\boldsymbol{E}$ are the magnetic flux density, the magnetic field intensity, the electric current density, the electric flux density and the electric field density, respectively.

The constitutive relations, which define the relationship between the field quantities in a linear, homogeneous, and isotropic medium are

$$\boldsymbol{B} = \mu \boldsymbol{H} \tag{2-5}$$

$$\boldsymbol{J} = \sigma \boldsymbol{E} \tag{2-6}$$

$$\boldsymbol{D} = \varepsilon \boldsymbol{E} \tag{2-7}$$

where μ, σ, and ε are the permeability, the conductivity and the permittivity, respectively.

In Quasi static field, the displacement current in Eq. (2-1) is negligible. So Eq. (2-1) becomes:

$$\mathrm{rot}\,\boldsymbol{H} = \boldsymbol{J} \tag{2-8}$$

In this case, the displacement current $\boldsymbol{D}$ is removed from the Maxwell equations and the following equation for the continuity of current is considered in stead of Eq. (2-3).

$$\mathrm{div}\boldsymbol{J} = 0 \tag{2-9}$$

B. The fundamental equations of $\boldsymbol{A}$*–*ϕ *method* [24]

In this section, the fundamental equations of $\boldsymbol{A}$-ϕ method taking account of the eddy current will be given.

First, the magnetic vector potential $\boldsymbol{A}$ is introduced. It guarantees that the Maxwell magnetic divergence equation $\mathrm{div}\boldsymbol{B} = 0$ will always be satisfied if the flux density $\boldsymbol{B}$ is to be expressed in terms of an auxiliary vector $\boldsymbol{A}$ as:

$$\boldsymbol{B} = \mathrm{rot}\,\boldsymbol{A} \tag{2-10}$$

And when the current density $\boldsymbol{J}$ is expressed with the exciting current density $\boldsymbol{J_0}$ and eddy current $\boldsymbol{J_e}$, Eq. (2-8) becomes:

$$\mathrm{rot}\,\boldsymbol{H} = \boldsymbol{J}_0 + \boldsymbol{J}_e \tag{2-11}$$

Substitute Eqs. (2-5) and (2-9) in Eq. (2-10), it becomes:

$$\mathrm{rot}\left(\nu\,\mathrm{rot}\boldsymbol{A}\right) = \boldsymbol{J}_0 + \boldsymbol{J}_e \tag{2-12}$$

where ν is reluctivity.

Substitute Eq. (2-5) in Eq. (2-18), it becomes:

$$\mathrm{rot}\left(\boldsymbol{E} + \frac{\partial \boldsymbol{A}}{\partial t}\right) = 0 \tag{2-13}$$

$\boldsymbol{E}$ is expressed as:

$$\boldsymbol{E} = -\frac{\partial \boldsymbol{A}}{\partial t} - \mathrm{grad}\phi \tag{2-14}$$

where ϕ is electric scalar potential.

Substitute Eqs. (2-6) and (2-14) in Eq. (2-12), it becomes:

$$\mathrm{rot}\left(\nu\,\mathrm{rot}\boldsymbol{A}\right) = \boldsymbol{J}_0 - \sigma\left(\frac{\partial \boldsymbol{A}}{\partial t} + \mathrm{grad}\phi\right) \tag{2-15}$$

Substitute Eqs. (2-6) and (2-14) in Eq. (2-17), it become:

$$\mathrm{div}\left\{-\sigma\left(\frac{\partial \boldsymbol{A}}{\partial t} + \mathrm{grad}\phi\right)\right\} = 0 \tag{2-16}$$

Eqs. (2-15) and (2-16) are the fundamental equations of $\boldsymbol{A}$-ϕ method including eddy current.

In the region where the eddy current is not considered, the fundamental equation becomes:

$$\mathrm{rot}\left(\nu\,\mathrm{rot}\boldsymbol{A}\right) = \boldsymbol{J}_0 \tag{2-17}$$

2.2 Discretization by Fnite Element Method

In this section, the edge finite elements are introduced. The 1st-order hexahedral elements with twelve vector edges in global coordinate system (x, y, z) and local coordinate system (ξ, ψ, ζ) are shown in Fig. 2.1 [25-27].

The scalar shape functions N_i for node i in the nodal hexahedral finite element are defined in the local coordinate system and expressed as follows:

$$N_i = \frac{1}{8}\left(1+\xi_i\xi\right)\left(1+\eta_i\eta\right)\left(1+\zeta_i\zeta\right) \quad \left(\mathrm{i} = 1 \sim 8\right) \tag{2-18}$$

where the local coordinates ξ_i, η_i, ζ_i for the nodes are given in the Table 2.1.

The vector shape functions $\boldsymbol{N}_j$ for edge j in the edge hexahedral finite element are

defined in the local coordinate system and expressed as follows:

$$\boldsymbol{N}_j = \begin{cases} \frac{1}{8}(1+\eta_j\eta)(1+\zeta_j\zeta)\,\mathrm{grad}\xi & (\mathrm{j}=1\sim4) \\ \frac{1}{8}(1+\zeta_j\zeta)(1+\xi_j\xi)\,\mathrm{grad}\eta & (\mathrm{j}=5\sim8) \\ \frac{1}{8}(1+\xi_j\xi)(1+\eta_j\eta)\,\mathrm{grad}\zeta & (\mathrm{j}=9\sim12) \end{cases} \tag{2-19}$$

where the local coordinates ξ_i, η_i, ζ_i for the edges are given in the Table 2.2.

The relation between the global and local coordinate systems is given by:

$$\begin{aligned} x &= \sum_{i=1}^{8} N_i x_i \\ y &= \sum_{i=1}^{8} N_i y_i \\ z &= \sum_{i=1}^{8} N_i z_i \end{aligned} \tag{2-20}$$

where N_i is the scalar shape function and x_i, y_i, z_i are the global coordinates of node i.

The scalar ϕ in one hexahedral element for the magnetic field analysis is obtained using the ϕ_i on each node of the element as follows:

$$\phi = \sum_{i=1}^{8} N_i \phi_i \tag{2-21}$$

The vector $\boldsymbol{A}$ in one hexahedral element for the magnetic field analysis is obtained using the A_j on each edge of the element as follows:

$$\boldsymbol{A} = \sum_{j=1}^{12} \boldsymbol{N}_j A_j \tag{2-22}$$

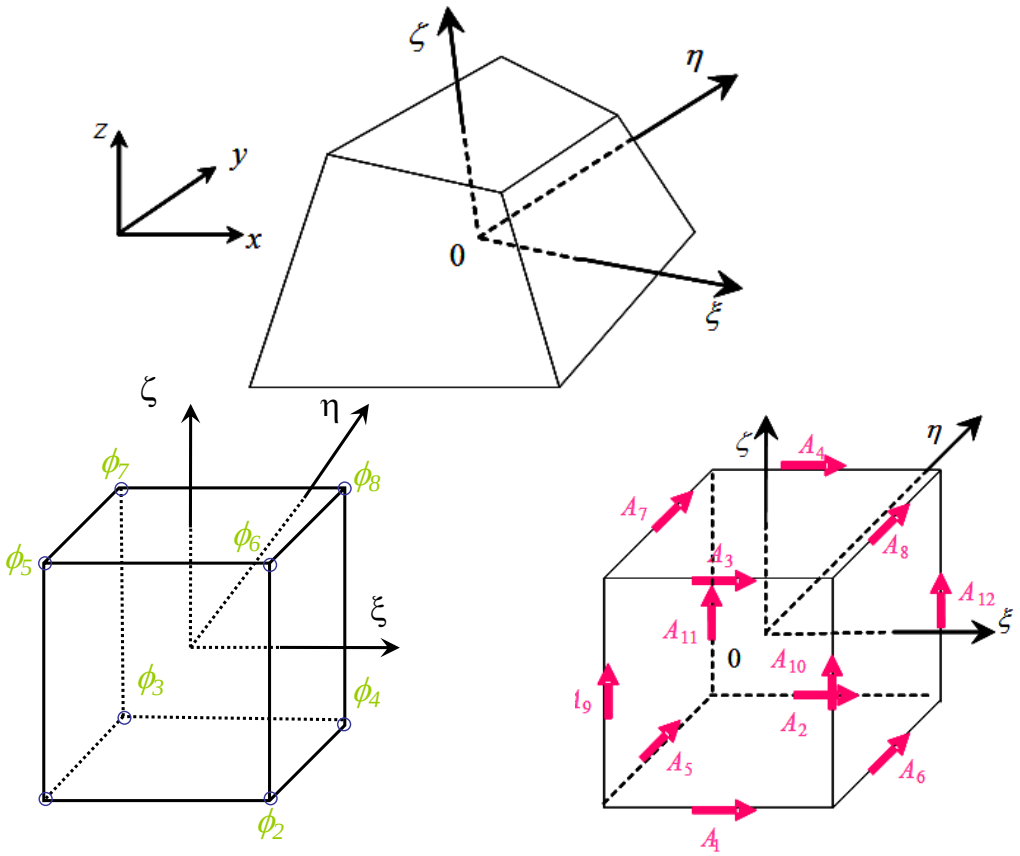

Fig. 2.1.1st-order hexahedral element. (a) Global coordinate system (x, y, z), (b) Local coordinate system (ξ, ψ, ζ): (i) for ϕ, and (ii) for edge element.

Table 2.1 Local coordinates for nodes.

Node number i	ξ_i	η_i	ζ_i
1	−1	−1	−1
2	1	−1	−1
3	−1	1	−1
4	1	1	−1
5	−1	−1	1
6	1	−1	1
7	−1	1	1
8	1	1	1

Table 2.2 Local coordinates for edges.

Edge number k	ξ_k	η_k	ζ_k
1	—	−1	−1
2	—	1	−1
3	—	−1	1
4	—	1	1
5	−1	—	−1
6	1	—	−1
7	−1	—	1
8	1	—	1
9	−1	−1	—
10	1	−1	—
11	−1	1	—
12	1	1	—

The integration expressed by x, y, z in the global coordinate system corresponds to that expressed by ξ, η, ζ in the local coordinate system as follows:

$$\int dxdydz = \int |\mathbf{J}| d\xi\xi d\eta d \tag{2-23}$$

where $\mathbf{J}$ is the Jacobian matrix expressed as:

$$\mathbf{J} = \begin{bmatrix} \frac{\partial x}{\partial \xi} & \frac{\partial y}{\partial \xi} & \frac{\partial z}{\partial \xi} \\ \frac{\partial x}{\partial \eta} & \frac{\partial y}{\partial \eta} & \frac{\partial z}{\partial \eta} \\ \frac{\partial x}{\partial \zeta} & \frac{\partial y}{\partial \zeta} & \frac{\partial z}{\partial \zeta} \end{bmatrix}, \tag{2-24}$$

In this section, the discretization for fundamental equations of the electromagnetic field analysis using the edge hexahedral element is explained.

By applying the weighted residual Galerkin method to Eq. (2-23) and (2-24), the

following residual equations can be obtained [28-30]:

$$\boldsymbol{G}_i = \iiint_V \boldsymbol{N}_i \bullet \left\{ \mathrm{rot}(\nu\, \mathrm{rot}\boldsymbol{A}) - \boldsymbol{J}_0 + \sigma\left(\frac{\partial \boldsymbol{A}}{\partial t} + \mathrm{grad}\phi \right) \right\} dxdydz = 0 \tag{2-25}$$

$$\boldsymbol{G}_{di} = \iiint_V \boldsymbol{N}_i \mathrm{div}\left\{ \sigma\left(\frac{\partial \boldsymbol{A}}{\partial t} + \mathrm{grad}\phi \right) \right\} dxdydz = 0 \tag{2-26}$$

The first term in Eq. (2-26) can be changed as follows:

$$\iiint_V \boldsymbol{N}_i \bullet \mathrm{rot}(\nu\, \mathrm{rot}\boldsymbol{A})\, dxdydz$$

$$= \iiint_V \left[\mathrm{div}\{\nu\, \mathrm{rot}\boldsymbol{A} \times \boldsymbol{N}_i\} + (\nu\, \mathrm{rot}\boldsymbol{A}) \bullet (\mathrm{rot}\, \boldsymbol{N}_i) \right] dxdydz$$

$$= \iiint_V (\mathrm{rot}\, \boldsymbol{N}_i) \bullet (\nu\, \mathrm{rot}\boldsymbol{A})\, dxdydz - \iint_S \{\boldsymbol{N}_i \times (\nu\, \mathrm{rot}\boldsymbol{A})\} \bullet \boldsymbol{n}\, dS$$

$$= \iiint_V (\mathrm{rot}\, \boldsymbol{N}_i) \bullet (\nu\, \mathrm{rot}\boldsymbol{A}) dxdydz - \iint_S \boldsymbol{N}_i \bullet \{(\nu\, \mathrm{rot}\boldsymbol{A}) \times \boldsymbol{n}\} dS \tag{2-27}$$

where S is the boundary of V, $\boldsymbol{n}$ is the outward normal vector of S. In the proceeding above, the following vector operations and the Gauss's theory are used:

$$\mathrm{div}(\boldsymbol{A} \times \boldsymbol{B}) = \boldsymbol{B} \cdot \mathrm{rot}\boldsymbol{A} - \boldsymbol{A} \cdot \mathrm{rot}\boldsymbol{B} \tag{2-28}$$

$$\boldsymbol{A} \cdot (\boldsymbol{B} \times \boldsymbol{C}) = \boldsymbol{B} \cdot (\boldsymbol{C} \times \boldsymbol{A}) = \boldsymbol{C} \cdot (\boldsymbol{A} \times \boldsymbol{B}) \tag{2-29}$$

The right term of Eq. (2-28) is zero to satisfy the weak boundary condition of $\boldsymbol{H}$ in the tangential direction. And then $\boldsymbol{G}_i$ becomes:

$$\boldsymbol{G}_i = \iiint_V \left[(\mathrm{rot}\, \boldsymbol{N}_i) \bullet (\nu\, \mathrm{rot}\boldsymbol{A}) - \boldsymbol{N}_i \bullet \boldsymbol{J}_0 + \boldsymbol{N}_i \bullet \left\{ \sigma\left(\frac{\partial \boldsymbol{A}}{\partial t} + \mathrm{grad}\phi \right) \right\} \right] dxdydz \tag{2-30}$$

The exciting current $\boldsymbol{J}_0$ in the element is expressed as follows by using the vector shape function $\boldsymbol{N}_i$ in Eq. (2-21).

$$\boldsymbol{J}_0 = \sum_{i=1}^{12} \boldsymbol{N}_i \boldsymbol{J}_{0i} \tag{2-31}$$

And

$$\mathrm{rot}\boldsymbol{A} = \mathrm{rot}\left(\sum_{\boldsymbol{j}=1}^{12} \boldsymbol{N}_{\boldsymbol{j}}\boldsymbol{A}_{\boldsymbol{j}}\right) = \sum_{\boldsymbol{j}=1}^{12}\left(\mathrm{rot}\,\boldsymbol{N}_{\boldsymbol{j}}\right)\boldsymbol{A}_{\boldsymbol{j}} \tag{2-32}$$

And

$$\mathrm{grad}\phi = \mathrm{grad}\left(\sum_{k=1}^{8} N_k\phi_k\right) = \sum_{k=1}^{8}\left(\mathrm{grad}N_k\right)\phi_k \tag{2-33}$$

Substitute Eqs. (2-31), (2-32), and (2-33) to Eq. (2-30), $\boldsymbol{G}_i$ becomes:

$$\begin{aligned} G_i = {} & \iiint_V \left[\left(\mathrm{rot}\,\mathbf{N_i}\right)\bullet\left(\nu\sum_{j=1}^{12}\mathrm{rot}N_j\mathrm{A_j}\right)\right]\mathrm{dxdydz} - \iiint_V \mathbf{N_i}\bullet\sum_{j=1}^{12}N_j\mathbf{J_{0}}_j\,\mathrm{dxdydz} \\ & + \iiint_V \mathbf{N_i}\bullet\left\{\sigma\left(\frac{\partial\sum_{j=1}^{12}N_j\mathbf{A}_j}{\partial t} + \sum_{j=1}^{8}\mathrm{grad\,N}_j\,\phi_j\right)\right\}\mathrm{dxdydz} \\ = {} & \sum_{j=1}^{12}\iiint_V \nu\left(\mathrm{rot}\,\mathbf{N_i}\right)\bullet\left(\mathrm{rot}N_j\right)\mathrm{dxdydz}\,\mathbf{A}_j - \sum_{j=1}^{12}\iiint_V \mathbf{N_i}\bullet N_j\,\mathrm{dxdydz}\,\mathbf{J_{0}}_j \\ & + \sum_{j=1}^{12}\iiint_V \sigma\mathbf{N_i}\bullet N_j\,\mathrm{dxdydz}\frac{\partial\mathbf{A}_j}{\partial\,\mathrm{t}} + \sum_{j=1}^{8}\iiint_V \sigma\mathbf{N_i}\bullet\mathrm{grad\,N}_j\,\mathrm{dxdydz}\phi_j \end{aligned} \tag{2-34}$$

In order to calculate the integration of the element, we should change the coordinate system from global to local, then $\boldsymbol{G}_i$ becomes:

$$\begin{aligned} G_i = {} & \sum_{V}\sum_{j=1}^{12}\int_{-1}^{1}\int_{-1}^{1}\int_{-1}^{1}\nu\left(\mathrm{rot}\,\boldsymbol{N_i}\right)\bullet\left(\mathrm{rot}N_j\right)|\mathrm{J}|\,\mathrm{d}\xi\mathrm{d}\eta\mathrm{d}\,A_j \\ & - \sum_{V}\sum_{j=1}^{12}\int_{-1}^{1}\int_{-1}^{1}\int_{-1}^{1}\boldsymbol{N_i}\bullet N_j|\mathrm{J}|\,\mathrm{d}\xi\mathrm{d}\eta\mathrm{d}\,\boldsymbol{J_0}_j \\ & + \sum_{V}\sum_{j=1}^{12}\int_{-1}^{1}\int_{-1}^{1}\int_{-1}^{1}\sigma\boldsymbol{N_i}\bullet N_j|\mathrm{J}|\,\mathrm{d}\xi\mathrm{d}\eta\mathrm{d}\frac{\partial A_j}{\partial\,\mathrm{t}} \\ & + \sum_{V}\sum_{j=1}^{8}\int_{-1}^{1}\int_{-1}^{1}\int_{-1}^{1}\sigma\boldsymbol{N_i}\bullet\mathrm{grad\,N}_j|\mathrm{J}|\,\mathrm{d}\xi\mathrm{d}\eta\,\zeta\phi_j \end{aligned} \tag{2-35}$$

where $\sum_{V}$ means the total elements in volume *V*. And by using the Gauss's numeric integration with two integration points, $\boldsymbol{G}_i$ becomes:

$$
\begin{aligned}
G_i = & \sum_V \sum_{j=1}^{12} \sum_{n_\xi=1}^{2} \sum_{n_\eta=1}^{2} \sum_{n_\zeta=1}^{2} \mathrm{W}_{n\xi}\, \mathrm{W}_{n\eta}\, \mathrm{W}_{n\zeta} |\mathrm{J}| \times \left\{ \nu (\mathrm{rot}\, \boldsymbol{N_i}) \bullet (\mathrm{rot} N_j) A_j \right\} \\
& - \sum_V \sum_{j=1}^{12} \sum_{n_\xi=1}^{2} \sum_{n_\eta=1}^{2} \sum_{n_\zeta=1}^{2} \mathrm{W}_{n\xi}\, \mathrm{W}_{n\eta}\, \mathrm{W}_{n\zeta} |\mathrm{J}| \times \left(\boldsymbol{N_i} \bullet N_j \boldsymbol{J_{0j}} \right) \\
& + \sum_V \sum_{j=1}^{12} \sum_{n_\xi=1}^{2} \sum_{n_\eta=1}^{2} \sum_{n_\zeta=1}^{2} \mathrm{W}_{n\xi}\, \mathrm{W}_{n\eta}\, \mathrm{W}_{n\zeta} |\mathrm{J}| \times \left(\sigma \boldsymbol{N_i} \bullet N_j \frac{\partial A_j}{\partial \mathrm{t}} \right) \\
& + \sum_V \sum_{j=1}^{8} \sum_{n_\xi=1}^{2} \sum_{n_\eta=1}^{2} \sum_{n_\zeta=1}^{2} \mathrm{W}_{n\xi}\, \mathrm{W}_{n\eta}\, \mathrm{W}_{n\zeta} |\mathrm{J}| \times \left(\sigma \boldsymbol{N_i} \bullet \mathrm{grad}\, \mathrm{N_j} \phi_j \right)
\end{aligned}
\tag{2-36}
$$

where W_{n_ξ}, W_{n_η}, W_{n_ζ} is the weighted factor , W_1 and W_2 are all -0.577350269189626 and 0.577350269189626, respectively.

Eq. (2-27) is changed to:

$$
\begin{aligned}
\boldsymbol{G_{di}} = & -\iiint_V (\mathrm{grad} \boldsymbol{N_i}) \bullet \left\{ \sigma \left(\frac{\partial \boldsymbol{A}}{\partial t} + \mathrm{grad} \phi \right) \right\} dxdydz \\
& + \iint_S N_i \left\{ \sigma \left(\frac{\partial \boldsymbol{A}}{\partial t} + \mathrm{grad} \phi \right) \right\} \bullet \boldsymbol{n} dS
\end{aligned}
\tag{2-37}
$$

In the proceeding above, the following vector operation and the Gauss's theory are used.

$$
\mathrm{div}(f\boldsymbol{A}) = (\mathrm{grad}\, f) \bullet \boldsymbol{A} + f\, \mathrm{div} \boldsymbol{A} \tag{2-38}
$$

The second right term in Eq. (2-37) becomes zero to satisfy the electric conservation law weakly. So $\boldsymbol{G_{di}}$ becomes:

$$
\boldsymbol{G_{di}} = -\sum_{j=1}^{12} \iiint_V \sigma \mathrm{grad} \boldsymbol{N_i} \bullet \boldsymbol{N_j}\, dxdydz \frac{\partial \boldsymbol{A_j}}{\partial t} - \sum_{j=1}^{8} \iiint_V \sigma \mathrm{grad} \boldsymbol{N_i} \bullet \mathrm{grad}\, N_j\, dxdydz \phi_j \tag{2-39}
$$

By using the same numeric method as in Eq. (2-37) becomes:

$$G_{di} = -\sum_{V} \sum_{j=1}^{12} \sum_{n_\xi=1}^{2} \sum_{n_\eta=1}^{2} \sum_{n_\zeta=1}^{2} W_{n_\xi} W_{n_\eta} W_{n_\zeta} |J| \times \left(\sigma \mathrm{grad} \boldsymbol{N_i} \bullet N_j \frac{\partial \boldsymbol{A}_j}{\partial t} \right)$$
$$-\sum_{V} \sum_{j=1}^{8} \sum_{n_\xi=1}^{2} \sum_{n_\eta=1}^{2} \sum_{n_\zeta=1}^{2} W_{n_\xi} W_{n_\eta} W_{n_\zeta} |J| \times \left(\sigma \mathrm{grad} \boldsymbol{N_i} \bullet \mathrm{grad} N_j \phi_j \right) \quad (2\text{-}40)$$

2.3 Treatment for Eddy Current Term

In the transient analysis, the backward difference method is used for the time differentiation in eddy current term in Eq. (2-38).

The derivative of a function *f* at a point *t* is defined by the limit:

$$f'(t) = \lim_{h \to 0} \frac{f(t+h) - f(t)}{h} \quad (2\text{-}41)$$

Then a reasonable approximation for that derivative would be to take:

$$f'(t) = \frac{f(t+h) - f(t)}{h} \quad (2\text{-}42)$$

A backward difference uses the function values at *t* and *t* − *h*, instead of the values at *t* + *h* and *t*:

$$f'(t) = \frac{f(t) - f(t-h)}{h} \quad (2\text{-}43)$$

So the time differential term $\partial \boldsymbol{A}^{t+\Delta t} / \partial t$ using the backward differential method is expressed by:

$$\frac{\partial \boldsymbol{A}^{t+\Delta t}}{\partial t} = \frac{\boldsymbol{A}^{t+\Delta t} - \boldsymbol{A}^{t}}{\Delta t} \quad (2\text{-}44)$$

Because the differentiation term $\partial \boldsymbol{A}^{t+\Delta t} / \partial t$ is the tangential of *f* at point $t+\Delta t$ as indicated by the dashed curve in Fig. 2.2, so the $\boldsymbol{A}^{t+\Delta t}$ obtained is $\boldsymbol{A}^{t+\Delta t}*$, which is the approximated value of the magnetic vector potential at time $t+\Delta t$ as shown in Fig. 2.

2. However, if the time interval Δt is small enough, this error is negligible.

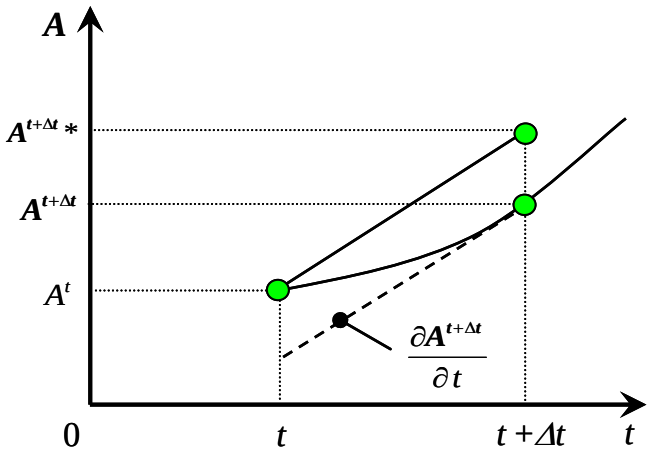

Fig. 2.2.Backward difference method.

In the linear ac steady state analysis, the phasor method is used for the time differentiation in eddy current term in Eq. (2-38). In this method, the time variation of the unknown *A(t)* is represented as follows:

$$A(t) = \dot{A}e^{j\omega t}, \tag{2-45}$$

where the upper script (.) denotes to the complex number which represents the phase difference. So, the time derivative term is represented as follows:

$$\frac{\partial A(t)}{\partial t} = j\omega\dot{A}e^{j\omega t}, \tag{2-46}$$

2.4 Eddy Current Loss Calculation

After the eddy current is obtained, eddy current loss *We* is calculated as follow:

$$W_e = \sum_{ie=1}^{N_{ei}} \left[\frac{\left| \boldsymbol{Je}^{(\mathrm{ie})} \right|}{\sigma *} \right] V^{(\mathrm{ie})} , \tag{2-47}$$

where $\boldsymbol{Je}^{(ie)}$ is the eddy current of the element *ie*, $V^{(ie)}$ is the volume of *ie*.

Chapter 3 Homogenization Technique of Laminated Core Under Rotational Flux

3.1 Introduction

In the finite element analysis of the magnetic field in an electric machine, the laminated cores are normally modeled by using a solid one and the eddy currents in the steel plates are neglected [31]. However, it seems that the eddy currents in the steel plates should not be neglected in some cases [9, 12, 32-33], such as in a machine driven by an inverter power supply in which the current has harmonics. Therefore, the homogenization technique, in which a laminated core is modeled by a three dimensional (3D) solid one (main-analysis) with anisotropic permeability and conductivity, and the permeability is determined by a one dimensional (1D) steel plate model (sub-analysis), which takes account of eddy currents in the steel plates and the structure of laminations [6], has already been proposed [7-8, 11-14]. In this method, the skin effect in steel plates and the effect of gaps between steel plates can be taken into account within practical computer costs. However, the proposed technique cannot be applied to motor cores because the rotational flux cannot be taken into account by using the 1D sub-analysis.

In my research, the 1D eddy current analysis of one steel plate (sub-analysis) in the proposed homogenization technique is expanded to a 3D sub-analysis which can take account of the direction of the flux density, in the linear magnetic field analysis for simplicity. To investigate the effectiveness of the developed homogenization

technique with the 3D sub-analysis, the proposed method is applied to a simple laminated core model under the rotational flux. The flux distribution, the eddy current distribution, and the eddy current loss obtained from using the proposed method are compared with those of the ordinary homogeneous solid core model with 1D steel plate model and the real laminated core model.

3.2 Method of Analysis

3.2.1 Laminated core and solid core model

A real laminated core and a solid core model are shown in Fig. 3.1. The core is constructed by laminating steel plates with permeability μ^* and conductivity σ^* in the z-direction, and it is modeled by using the solid core model with anisotropic effective permeabilities μ_x μ_y, and μ_z and conductivies σ_x, σ_y, and σ_z in this paper. The superscript (*) denotes the real quantities of the steel plates.

As both paths of the eddy currents, Je_{xy}^* and Je_{xy}, parallel to the plane of the steel plate, in the laminated and solid core models are the same, as shown in Fig3. 1, Je_{xy} is directly considered in the solid core model. Then, σ_x and σ_y are given by the following equation using the space factor F considering that the gaps between the steel plates are non-conductive:

$$\sigma_x = \sigma_y = F\sigma^* \quad , \tag{3-1}$$

On the other hand, the perpendicular components, $Je_z^*$and Je_z, of the eddy currents are much different in the two models shown in Fig. 3.1. Therefore, Je_z is not directly considered in the solid core model, but the effect of Je_z^* is considered in the process

of modifying μ^* to the effective permeabilities μ_x, μ_y and μ_z. Namely, the conductivity σ_z becomes zero as follows:

$$\sigma_z = 0 \quad , \tag{3-2}$$

The effective permeabilities taking account of the effect of Je_z*are determined by using the eddy current finite element analysis of one steel plate (called "sub-analysis").

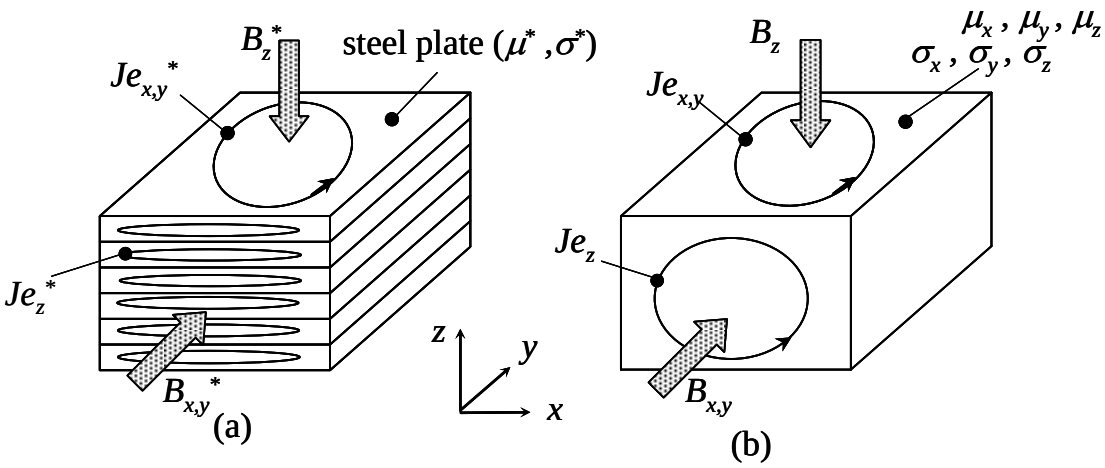

Fig.3.1.(a) Laminated core and (b) solid core models [8].

3.2.2 Flowchart

The flowchart for the proposed method is shown in Fig.3.2. The sub-analysis is carried out for each element *ie* of the solid core model (called "main-analysis"). The methods of main-analysis and sub-analysis are described below, respectively.

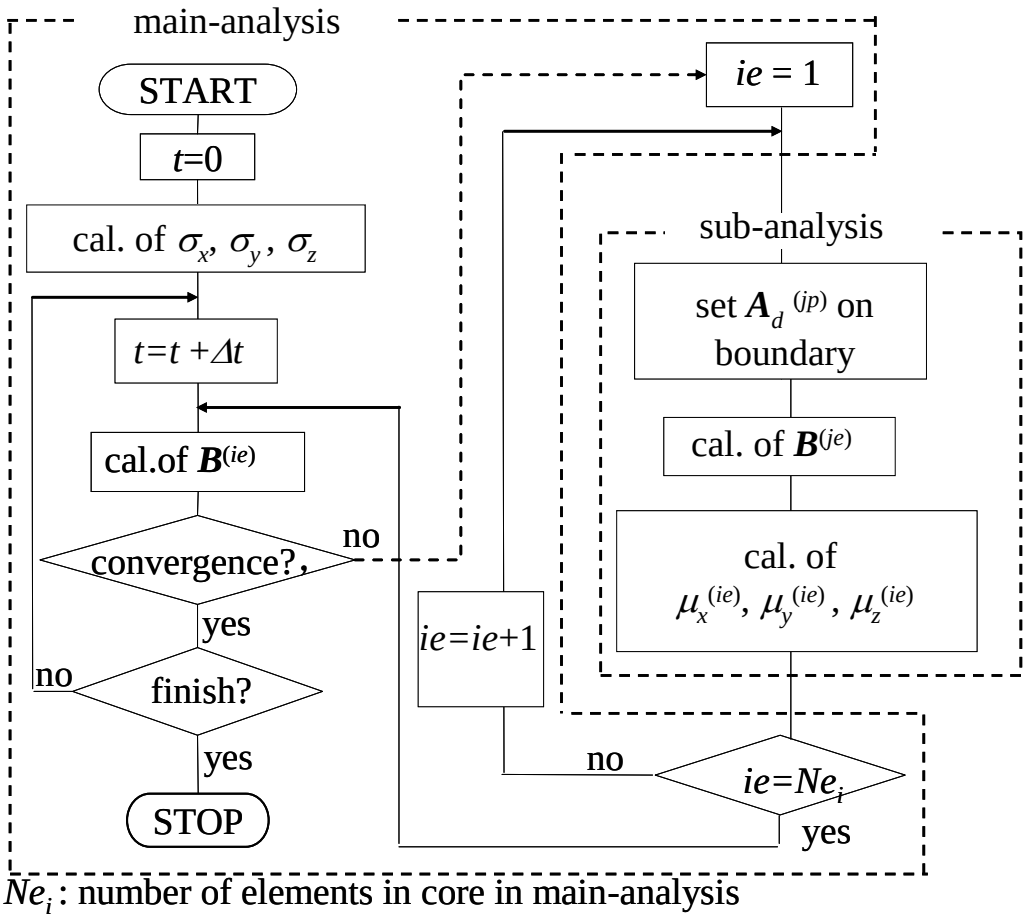

Fig.3.2. Flowchart of the proposed method [8].

3.2.3 Main-analysis

The 3D linear eddy current analysis with the first order edge finite elements of the solid core model is carried out. The fundamental equation is as follows:

$$\mathrm{rot}\left(\nu\ \mathrm{rot}\mathbf{A}\right) = -\sigma\left(\frac{\partial \mathbf{A}}{\partial t} + \mathrm{grad}\,\phi\right), \tag{3-3}$$

$$\mathrm{div}\left\{-\sigma\left(\frac{\partial \boldsymbol{A}}{\partial t} + \mathrm{grad}\,\phi\right)\right\} = 0, \tag{3-4}$$

where A and ϕ is the magnetic vector potential and the electric scalar potential,

respectively. σ is the anisotropic conductivity σ_x, σ_y, and σ_z as described above and is anisotropic ν_x, ν_y, and ν_z obtained from the sub-analysis explained in the next section.

The magnetic field is applied by the Dirichlet boundary condition in this paper. The simple iteration method is used for the convergence of the flux densities. The step-by-step method with the back-ward difference method is used for the time iteration.

3.2.4 Sub-analysis

In this section, the 1D sub-analysis used in the ordinary modeling homogenization is expanded into the 3D sub-analysis to take account of the rotational flux.

Fig. 3.3. shows the mesh for the 3D sub-analysis of one steel plate with thickness 2d, which is assumed to be infinite in the *x*-, *y*-directions. Only half region of one steel plate is analyzed due to symmetric. *je* and *jp* denote the element and node numbers in the sub-analysis. In the 3D sub-analysis, the *x*-, *y*-components $B_x^{(ie)}$,$B_y^{(ie)}$ of the flux density obtained from the main-analysis are imposed on the steel plate model, the *x*-, *y*- components $B_x^{(ie)}$,$B_y^{(ie)}$ of the flux density and $Je_x^{(je)}$, $Je_y^{(je)}$ of the eddy current density are calculated. The same method of magnetic field analysis with the main-analysis, but real σ^* and ν^* of the steel plates are used in the 3D sub-analysis. The *A* method neglecting ϕ in (3-3) is performed for the 3D sub-analysis. All *z*-component $A_z^{(jp)}$ of *A* is set to be zero in the whole region. The other components $A_{0x}^{(jp)}$, $A_{0y}^{(jp)}$ on the symmetric surface at $z = 0$ are also set to be zero, and $A_{dx}^{(jp)}$ and $A_{dy}^{(jp)}$determined by the following equations using $B_x^{(ie)}$and

$B_y^{(ie)}$obtained from the main-analysis are imposed on the upper surface at $z = d$:

$$A_{dx}^{(jp)} = B_y^{(ie)} d\,, \tag{3-5}$$

$$A_{dy}^{(jp)} = -B_x^{(ie)} d\,, \tag{3-6}$$

The periodic boundary conditions are applied on each corresponding side surfaces.

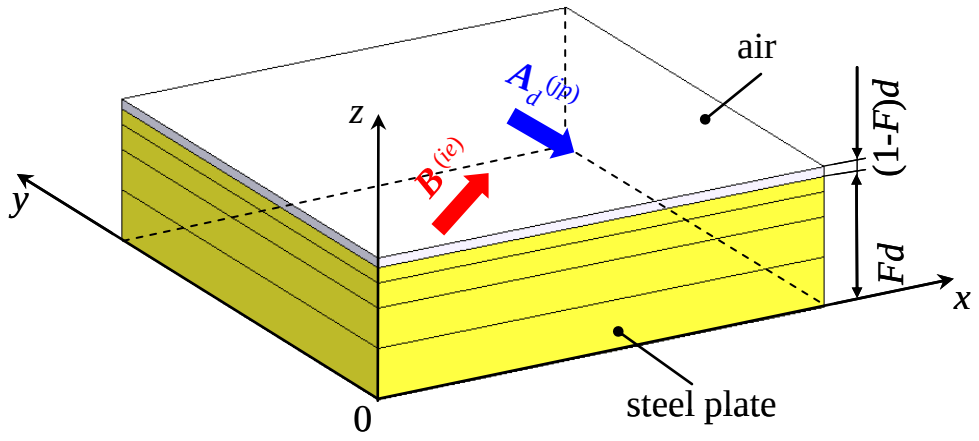

Fig. 3.3.Mesh for the 3D steel plate model (3D sub-analysis, half region)

The time differential term is discretized by the backward difference method. Therefore, for the calculation at the instant $t+\Delta t$, the potentials $A_x^{(jp)}$ and $A_y^{(jp)}$ at each node *jp* in the sub-analysis are stored for each element *ie* in the main-analysis at the instant *t*.

Finally, the permeabilities $\mu_x^{(ie)}$ and $\mu_y^{(ie)}$ given back to the main-analysis is determined by the following equation:

$$\mu_x^{(ie)} = B_x^{(ie)} \Big/ H_x^{(jair)}\,, \tag{3-7}$$

$$\mu_y^{(ie)} = B_y^{(ie)} \Big/ H_y^{(jair)}\,, \tag{3-8}$$

where $H_x^{(jair)}$ and $H_y^{(jair)}$ are the magnetic field strength in the air obtained from the sub-analysis. The permeability μ_z^{ie} is determined by the following equation so that the reluctances of real and solid core models coincide with each other in the *z*-direction:

$$\mu_z^{(ie)} = \frac{\mu^* \mu_0}{\mu^*(1-F) + \mu_0 F} \quad , \tag{3-9}$$

μ_z^{ie} is always not changed in the linear analysis.

3.2.5 Eddy Current Losses

In my research, the eddy current losses W_{eddy} in the laminated core are also evaluated. In the proposed method, the eddy currents $\boldsymbol{Je}^{*(ie)}$ (=$\boldsymbol{Je}^{(ie)}/F$) and $\boldsymbol{Je}^{*(je)}$ are obtained from the main- and sub- analyses, respectively. In order to calculate the eddy current losses, they should be added up with each other. Namely, the eddy current losses W_{eddy} are calculated by the following equation:

$$W_{eddy} = \sum_{ie=1}^{N_{ei}} \left(\frac{1}{d} \sum_{je=1}^{N_{ej}} \frac{\left| \boldsymbol{Je}_{\alpha}^{*(ie)} + \boldsymbol{Je}_{\beta}^{*(je)} \right|^2}{\sigma^*} l^{(je)} \right) V^{(ie)}, \tag{3-10}$$

where $l^{(je)}$ is the thickness of the element *je* in the sub-analysis. $V^{(ie)}$ is the volume of the element *ie* in the main-analysis. And N_{ej} is the number of elements in the conductive region in the sub-analysis.

3.3 Verification

3.3.1 Model description

As the real model analysis can not be carried out by the real motor due to a large number of elements，to investigate the effectiveness of the proposed 3D sub-analysis, the linear eddy current analysis of a simple laminated core model under the rotational flux shown in Fig. 3.4 is carried out. Only half region is shown due to symmetry in Fig. 3.4. The laminated core is constructed by laminating 4 sheets of steel plates (relative permeability: 2000, thickness: 0.5mm) in the *z*-direction, and the space factor *F* is equal to 0.96. The magnetic characteristic of the steel plates is assumed to be linear in this paper for simplicity. The laminated cores with dimensions *l* of 2000 mm, respectively, shown in Fig. 3.4 are analyzed. The uniform flux density *B* of 0.01T rotating anti-clockwisely at 1,670 rpm from *x*-direction to *y*-direction is applied as shown in Fig. 3.4.

The meshes of the real and solid core models with the first order edge finite elements are shown in the Figs. 3.5 and 3.6. The mesh near the upper surface of the solid core model and the 3D mesh for the sub-analysis in the proposed method are the same as that in the corresponding part of the real model. The total numbers of elements for the real and homogeneous solid core models are 9,747 and 3,610, respectively.

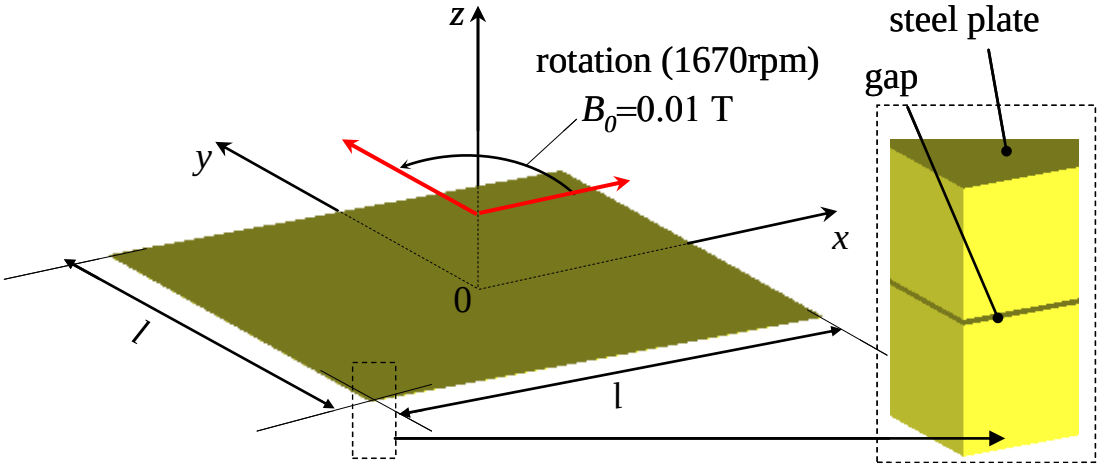

Fig. 3.4.Simple laminated core model (half region).

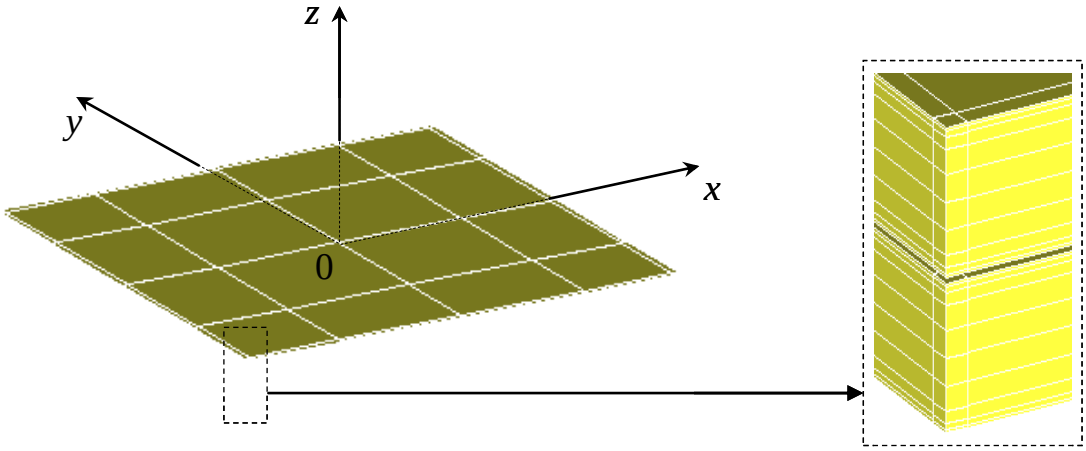

Fig. 3.5.Mesh of the real laminated core model (half region).

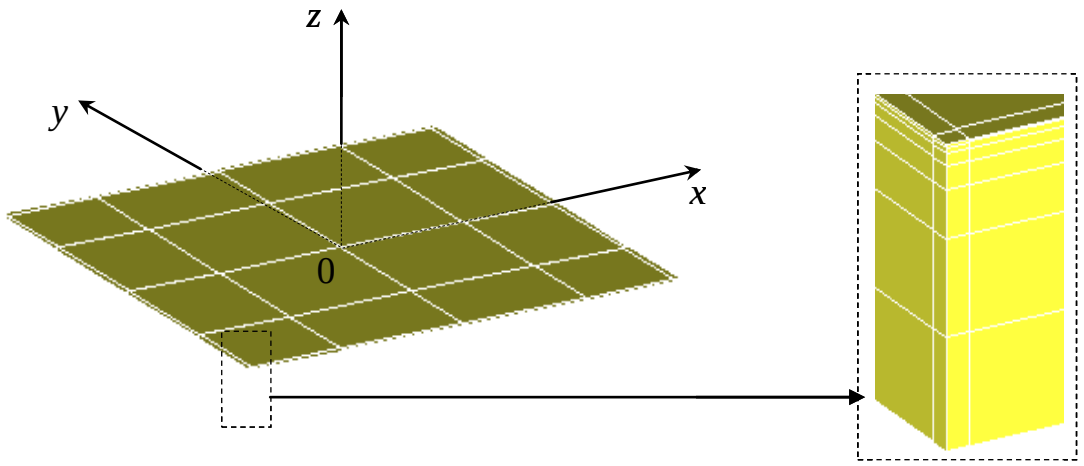

Fig.3.6. Mesh of the solid model (half region).

3.3.2 Analyzed Conditions

The linear transient analysis with only 9 steps at the time interval Δt of 1 ms is carried out. Namely, the applied flux density rotates at 10 deg. per step. The rotational flux densities are applied by using the Dirichlet and periodic boundary conditions of the A which are the same with those for the sub-analysis mentioned above in the real and solid models. No boundary condition for ϕ is given in the real model because the steel plates do not contact with any boundaries of analysis region. The Dirichlet boundary condition of ϕ is imposed on the symmetric surface $z = 0$ in the solid core model. For comparison, the ordinary 1Dsub-analysis method is also carried out.

3.3.3 Results and Discussion

In this section, the comparison between the real and homogeneous solid core models is carried out.

A. Flux Distribution

Fig. 3.7 shows the flux distributions in the upper surface of the laminated core at t = 9ms, when the applied flux density is in the y direction, obtained from the real model and the main-analysis of the proposed homogenized solid core model with the 3D sub-analysis. There is discrepancy at the corner of cores between both results. This is because the edge effect of the steel plate cannot be taken account of in the solid core model due to the assumption of infinity.

Fig.3. 8 and Fig.3. 9 shows the distributions and the error distributions of the average flux density in the upper steel plate at t = 9ms. As we can see in the Fig.3. 8, the average flux density in the upper steel obtained from two models are in good agreement with each other. The errors are within 1% as it was shown in the Fig.3. 9. Only at the corner, the errors are large, in the other place, the errors are almost 0.

Fig. 3.10 shows the distributions of y-component B_y of flux densities in the steel plate in the thickness direction at the center ($x = y = 0$) and the side (x =1000mm, $y = 0$). For reference, the homogenized model with 1D sub-analysis and the average values including gaps in the real model are also shown. The flux distributions obtained from both homogenized models with 1D and 3D sub-analyses are the same and they are in good agreement with the average values in the real model in this model.

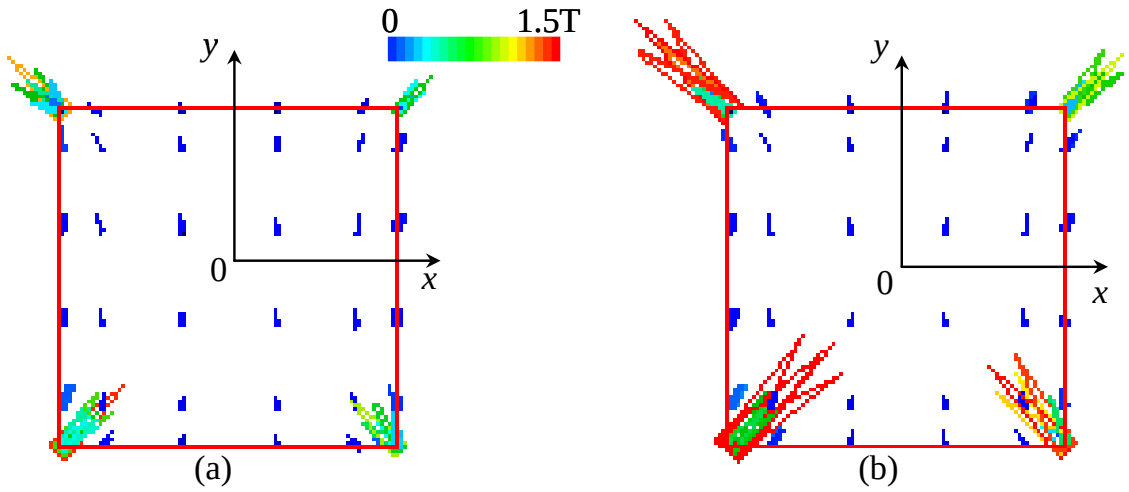

Fig. 3.7. Flux distributions in upper surface of core (z = 1mm, t = 9 ms): (a) real model, (b) main-analysis of solid model.

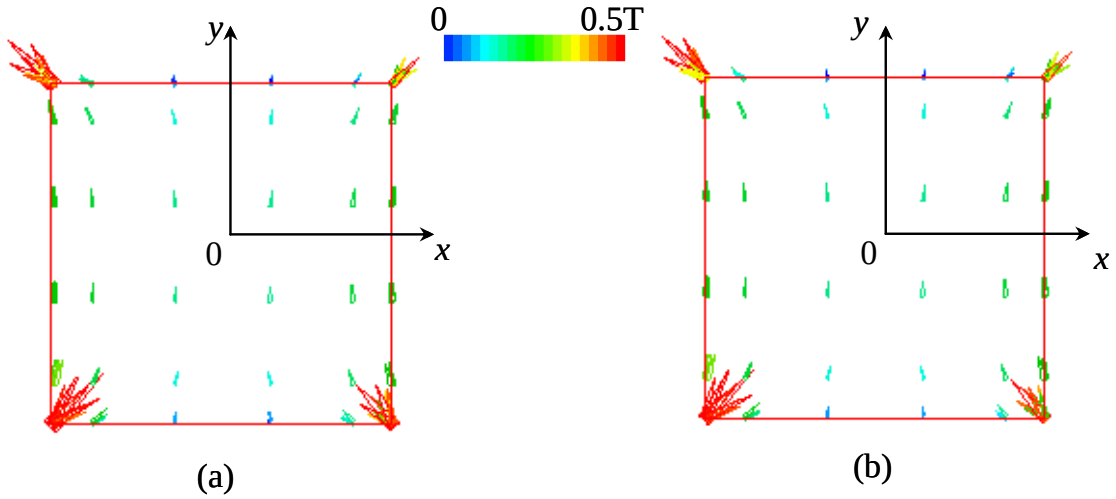

Fig. 3.8. Distributions of the average flux densities in the upper steel plate (t = 9 ms): (a) Real model, (b) Solid model.

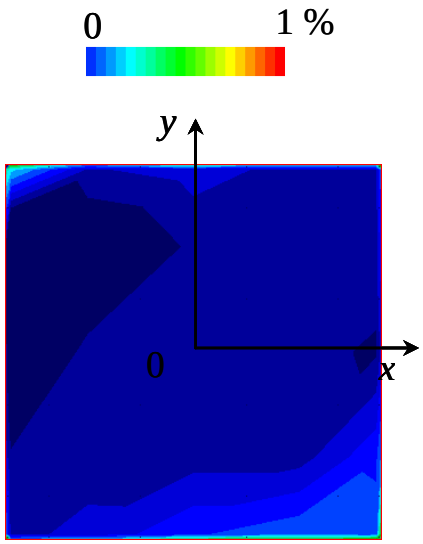

Fig. 3.9. Error distributions of the average flux densities in the upper steel plate (t = 9 ms)

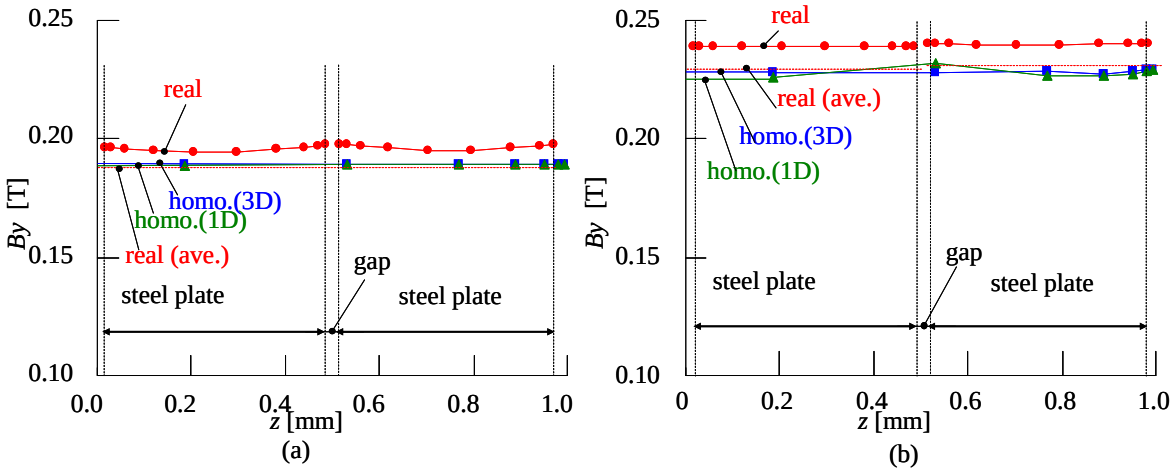

Fig. 3.10. Distributions of the y-component B_y of flux densities in the steel plate (t= 9 ms): (a) x=y=0, (b) x=1, y=0.

B. Eddy current distribution

Fig. 3.11 shows the eddy current distributions in the upper surface of the laminated core at t = 9 ms. The eddy current distribution obtained from the proposed method is much different from the real model, because the effect of the eddy current Je_z* in the steel plate is taken into account by using effective permeability but Je_z* is not directly calculated in the main-analysis of the solid core model.

However, when the eddy current densities is averaged in the steel plate, the distribution of the average eddy current densities obtained from the main-analysis of the solid model are in good agreement with that obtained from the real model as shown in Fig. 3.12 and Fig.3. 13. Fig. 3.12 and Fig.3. 13 are the distributions and the error distributions of the average eddy current densities in the upper steel obtained from the real model and the main-analysis of the solid model at t = 9ms, respectively. As it can be shown in the Fig.3. 13, the errors of the average eddy current density are within 1%. The same with the error distributions of the average flux densities, in the corner, the errors of the eddy current densities are larger compared with other region, the errors in the other places are almost 0.

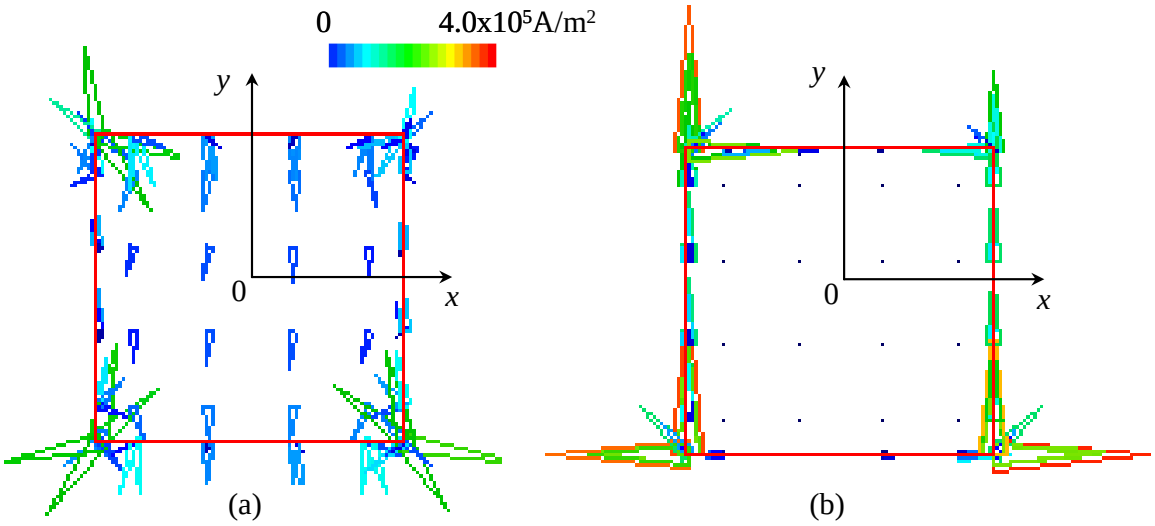

Fig. 3.11. Eddy current distributions in upper surface of core (z = 1mm, t = 9 ms): (a) Real model, (b) Main-analysis of solid model.

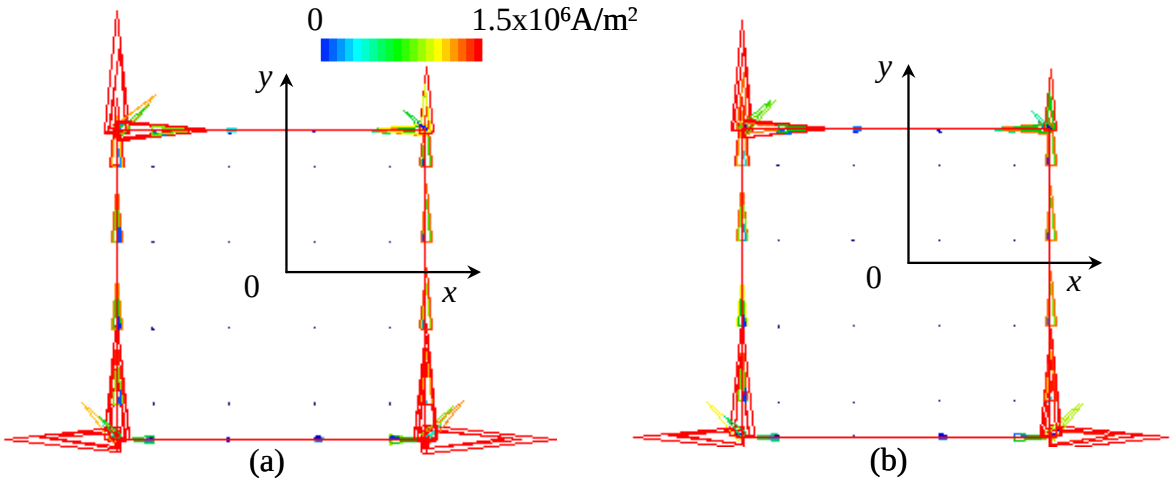

Fig. 3.12. Distributions of the average eddy current densities in the upper steel plate (t = 9 ms): (a) Real model, (b) Solid model.

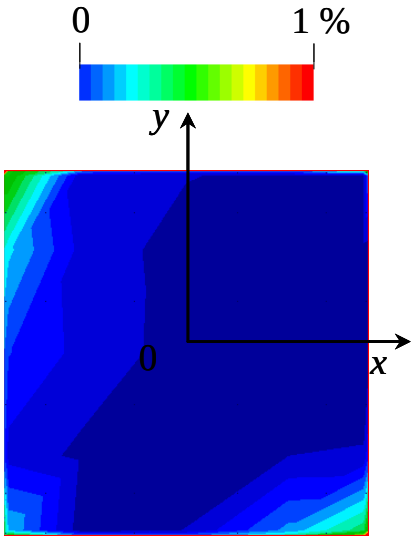

Fig. 3.13. Error distributions of the average eddy current densities in the upper steel plate (t = 9 ms).

C. Eddy current loss

Fig. 3.14 shows the distributions of eddy current loss densities *We* in the steel plate in the thickness direction at the center (x = y = 0) and the side (x =1000mm, y = 0). At the center of the steel plate, the eddy current loss densities obtained from the homogenized model with 3D sub-analysis are in good agreement with the average values in real model, whereas those obtained from the homogenized model with 1D sub-analysis are much smaller as Fig. 3.14 (a). This is because the eddy currents generated by rotating flux can not be considered in 1D sub-analysis. Therefore, 3D sub-analysis is required when the flux is rotating.

On the other hand, at the side of the steel plate, the eddy current loss densities obtained from both homogenized models with 3D and 1D sub-analyses are much different from those obtained from real model. This is because the edge effect does

not be taken account of in the homogenized model.

Fig. 3.15 shows the time variations of the eddy current loss *We* in the steel plates. The accuracy of the homogenized model can be improved by using the 3D sub-analysis compared with the 1D sub-analysis. Moreover, the eddy current loss *We* obtained from the homogenized model with 3D sub-analysis is in good agreement with those obtained from the real model because the effect of edge effect can be neglected in this model. Therefore, the effectiveness of the proposed 3D sub-analysis can be shown. However, a little error still occurs due to the neglect of the effect of the core edge in the 3D sub-analysis.

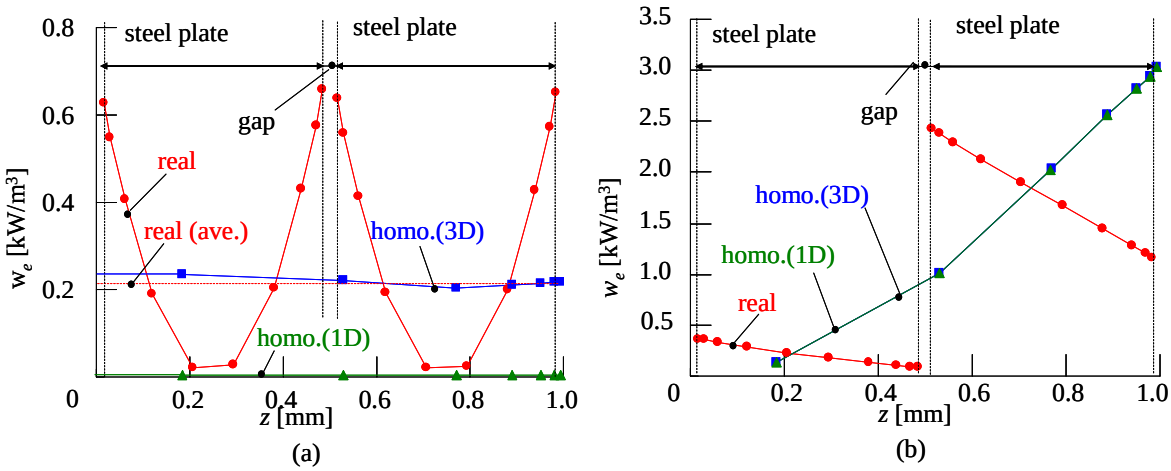

Fig. 3.14. Distributions of the eddy current loss densities we in the steel plate (t =9 ms): (a) x=y=0, (b) x=1, y=0.

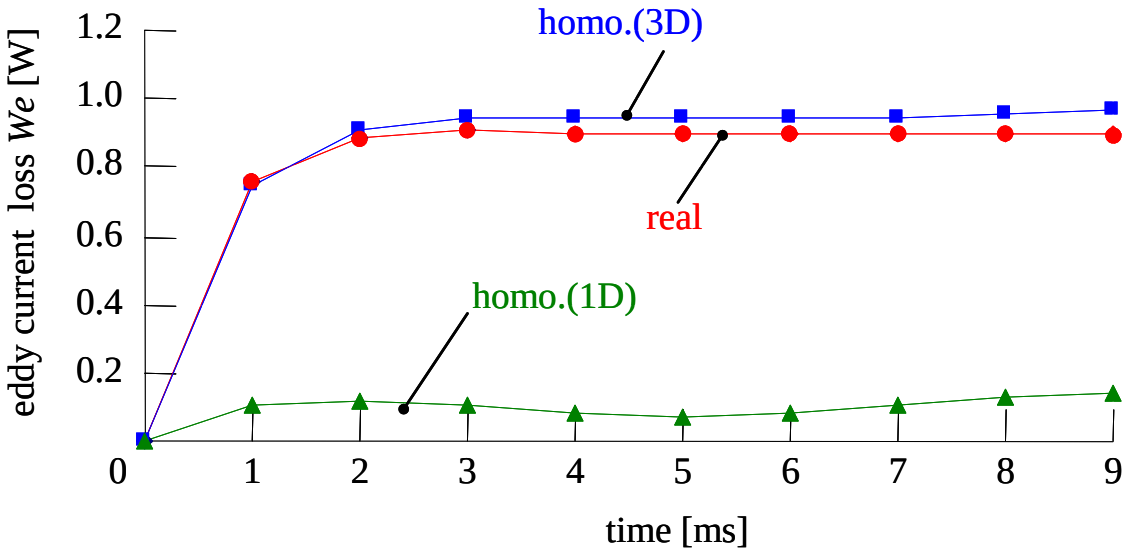

Fig.3.15. Time variation of the average eddy current losses.

D. CPU time

Table 3.1 shows Discretization Data and CPU time of the real laminated core and its homogenization model. As it was shown in the table, the CPU times for the real and homogenized models are 1477 and 1623 seconds @Intel Corei7, 3.4GHz. Compared with the real model, the number of elements of homogenized models is smaller as mentioned above but the CPU time is larger. This is because determining the permeability for the proposed homogenization technique requires three iterations for the linear problem. However, in the nonlinear case, the iterations are not a burden.

Table 3.1 Discretization data and CPU time of the real laminated core and its homogenization model.

Model	real	homogenization
Number of elements	9,747	3,610
Number of nodes	11,200	4,400
Number of edges	32,080	12,360
Number of unknowns	31,181	10,108
iterations	1	3
Total Memory requirements(MB)	16	5
Number o iterations of ICCG method*	6,790	2,314
Total CPU time (s)	1,477	1,623
In the nonlinear case	1	0.3

Computer used : Intel Core i7 3.4GHz
Convergence criterion for ICCG method : 10^{-10}

3.4 Summary

To apply the homogenization technique of laminated core taking account of eddy currents in the steel plates to motor cores, the 3D sub-analysis model of steel plate is proposed. The accuracy is much improved by the 3D sub-analysis compared with the ordinary 1D sub-analysis. However, the error due to the edge effect of the core occurs because the steel plate is assumed to be infinite in the proposed 3D sub-analysis.

The 3D sub-analysis model taking account of the nonlinearity and the edge effect of steel plate will be developed and applied to an actual motor in future.

Chapter 4 Homogenization Technique of Model Composed of Distributed Component

4.1 Introduction

Great efforts toward the finite element modeling and huge computation costs are required in the magnetic field analyses of models composed of distributed components, such as a building [3]. The homogenization techniques are effective to circumvent these problems by modeling the distributed components using a homogeneous body [16]. Several homogenization techniques has already been proposed [17-20]. In magnetostatic analyses, the homogenization technique using effective permeabilities based on the energy conservation has already been proposed [19]. It has been applied to the analyses of the magnetic disturbances of buildings [20] and the magnetic shielding performances of open-type magnetically shielded rooms composed of magnetic square cylinders [21]. On the other hand, the homogenization technique for a laminated core taking account of the eddy currents in the steel plates using effective permeabilities determined by using one-dimensional (1D) eddy current analysis of one steel sheet has also been proposed [7-8, 11, 14]. However, the homogenization technique for a periodic conductive components taking account of eddy currents seems not established. This is because a 2D or 3D eddy current analysis of the cell model is required to determine the effective permeability, moreover, the eddy current distributions are affected by insulation and conduction between conductive components.

In my research，homogenization techniques for periodic conductive and non-magnetic components are investigated using models of open-type electromagnetic shielding walls piled using square cylinders with and without gaps in linear ac steady-state eddy current problems. Two homogenization techniques are examined in both models. One is the technique homogenized by using a magnetic body with effective anisotropic complex permeability and without eddy currents. This technique is based on that for the homogenization of laminated cores [7, 8, 11-14]. The other is the technique homogenized by using a non-magnetic conductive body with modified anisotropic conductivity. To clarify the suitable technique for each model with or without gaps, the shielding effects obtained using both homogenization techniques are compared with those obtained using the real models. Moreover, the methods for determining effective permeability and modified conductivity in both techniques are proposed and verified.

4.2 Homogenization Techniques

4.2.1 Model description

In this thesis, the real model of an open-type shielding wall piled with conductive and non-magnetic square cylinders shown in Fig. 4.1(a) is investigated. Only 1/8 of the whole model is analyzed due to symmetry. The shielding effect of the wall is calculated under a uniform sinusoidal magnetic filed B_{0x} of 1T applied in x direction. Two models, in which cylinders are piled up with gaps G of 2 mm and without, are used. In the model without gaps, length L, width W, and thickness t of the cylinders are 10, 100, and 4 mm, respectively, and the frequency f of the magnetic field is chosen as 50 Hz. If the same L and f are applied for the model with gaps, the

shielding effect becomes too small. Therefore, L and f are changed to 50 mm and 500 Hz in the model with gaps. The conductivity σ and relative permeability μ_s of the cylinders are 2×107 S/m and 1, respectively.

Fig. 4.1 (b) shows the homogenization model with the same outer dimension of the real model. In this thesis, two homogenization techniques are applied: using a magnetic, non-conductive body and a conductive, non-magnetic body.

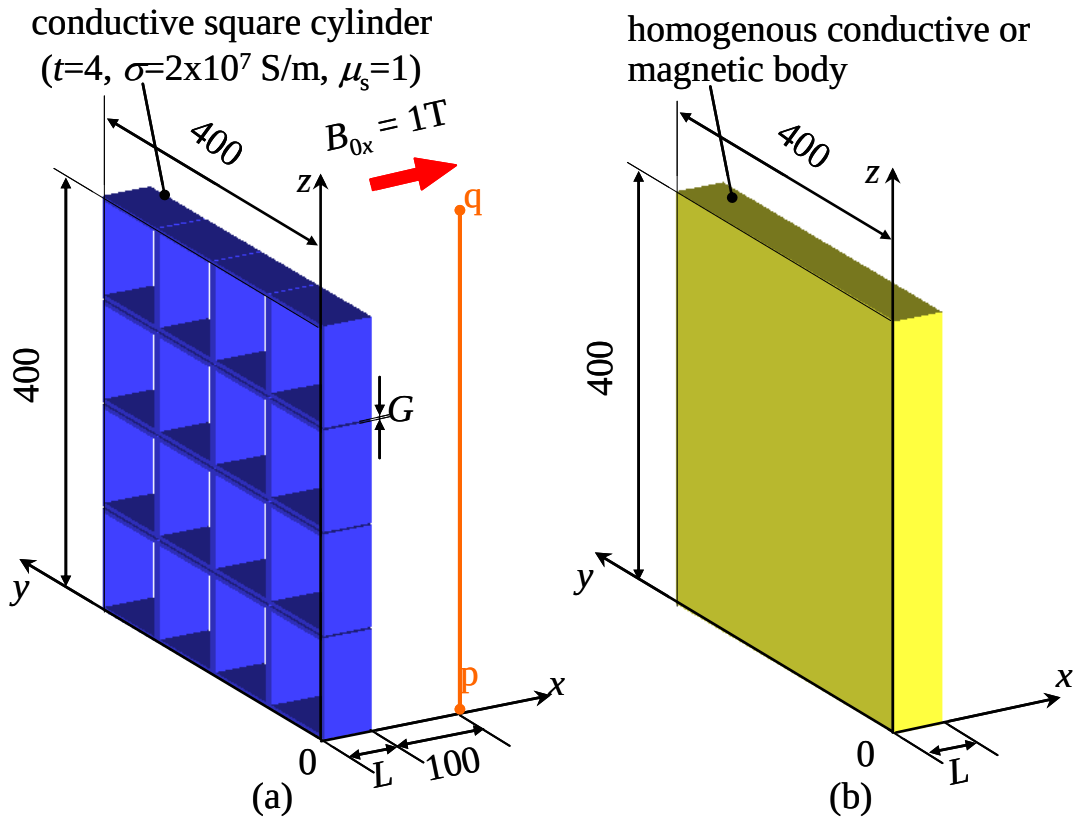

Fig.4. 1. Shielding wall, (a) real model and (b) homogenized model (1/8 region).

4.2.2 Eddy Current Analysis of Real Model

For the real model, linear ac steady-state eddy current analysis is performed using the 1st order brick edge finite element method with A-ϕ method (A: magnetic vector

potential, ϕ: electric scalar potential) and the phasor method with complex variables [37]. The fundamental equations are

$$\mathrm{rot}\left(\nu\,\mathrm{rot}\boldsymbol{A}^*\right) = -\sigma\left(j\omega\boldsymbol{A}^* + \mathrm{grad}\phi^*\right) \quad , \tag{4-1}$$

$$\mathrm{div}\left\{-\sigma\left(j\omega\boldsymbol{A}^* + \mathrm{grad}\phi^*\right)\right\} = 0 \, , \tag{4-2}$$

where the superscript (*) indicates complex variables, ω and ν are the angular frequency and the reluctivity, respectively.

Due to the eddy currents, the *x*, *y*, and *z* components of *B* have different phase angles, therefore, the maximum absolute flux density |*B*| for evaluation is calculated as follows.

$$|B| = \sqrt{1/2\left(|\dot{B}_x^2| + |\dot{B}_y^2| + |\dot{B}_z^2| + |\dot{B}_x^2 + \dot{B}_y^2 + \dot{B}_z^2|\right)} \, , \tag{4-3}$$

4.2.3 Homogeneous Magnetic Body

In this technique, the real model is homogenized by the magnetic, non-conductive body and the magnetostatic analysis is performed. The effect of the eddy currents is considered by using the effective anisotropic complex permeability μ_h*. The fundamental equation is

$$\mathrm{rot}\left(\nu_h * \mathrm{rot}\boldsymbol{A}^*\right) = 0 \quad , \tag{4-4}$$

The post-processing of ***A*** and ***B*** are the same with above.

4.2.4 Homogeneous Conductive Body

In this technique, the real model is homogenized by using the conductive and non-magnetic body with the modified anisotropic conductivity σ_h. The eddy current analysis with σ_h instead of σ in the equation (4-1) and (4-2) is performed.

4.3 Verification for Homogenization of Real Model With Gaps

4.3.1 Model description

Fig.4.1 shows the real model with gaps of 2 mm ,length *L*, width *W*, and thickness *t* of the cylinders are 50, 100, and 4 mm, *f* is 500 Hz in the model. The conductivity σ and relative permeability μ_s of the cylinders are 2×107 S/m and 1, respectively.

4.3.2 Selection of suitable technique

First, to clarify the suitable homogenization technique for the real model with gaps, the distributions $|B|_{p\text{-}q}$'s of the maximum absolute flux densities on the line *p*-*q* shown in Fig. 4.1, which is assumed as the evaluation line, obtained using both homogenization techniques are compared with that using the real model.

In this section, the effective permeability μ_{hp}* of the magnetic body and the modified conductivity σ_{hp} of the conductive body are isotropic and they are determined so that the maximum absolute flux densities $|B|_p$'s at point *p* obtained from both homogenization techniques coincide with that obtained from the real model.

Fig. 4.2 shows $B_{p\text{-}q}$'s obtained using the real model and its homogeneous magnetic and conductive bodies. The determined relative permeability μ_{hpr}* and conductivity σ_{hp} are denoted in Fig. 4.2. In the technique with the conductive body, large error occurs because the eddy current path in the homogeneous conductive body is much different from that in the real model shown in Fig. 4.3 due to the gaps. Fig. 4.2 also shows that the homogenization technique with the magnetic body is suitable for the

real model with gaps.

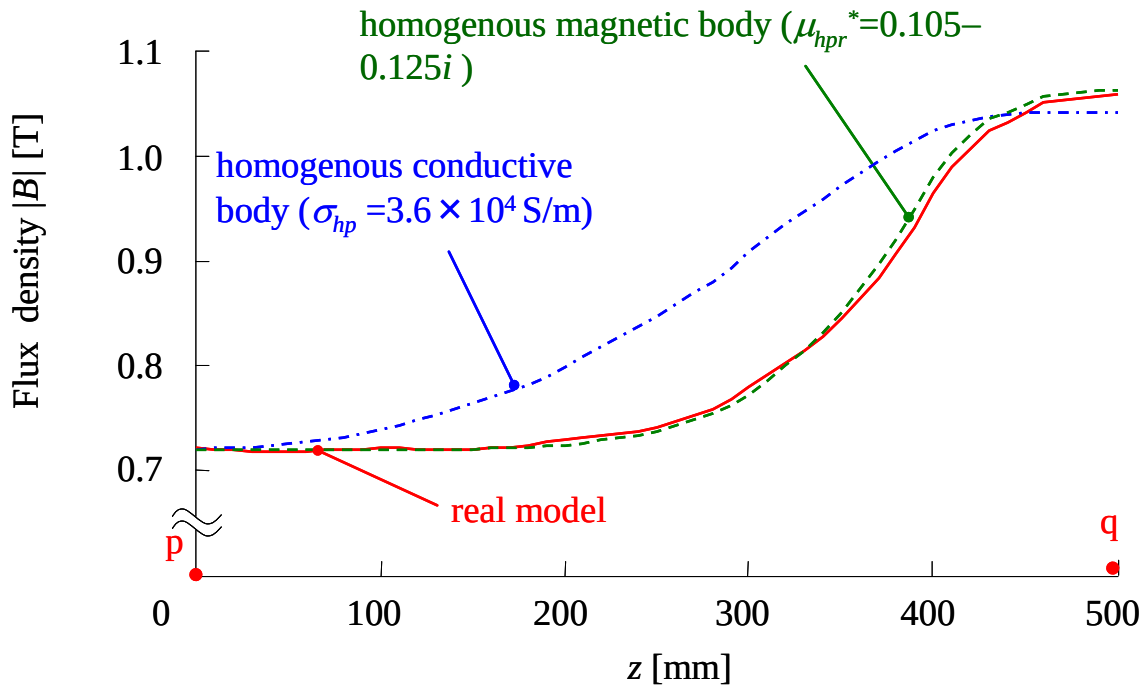

Fig. 4.2. Flux distribution on line p-q obtained using the real model with gaps and its homogeneous bodies (G = 2, L = 50, f = 500Hz).

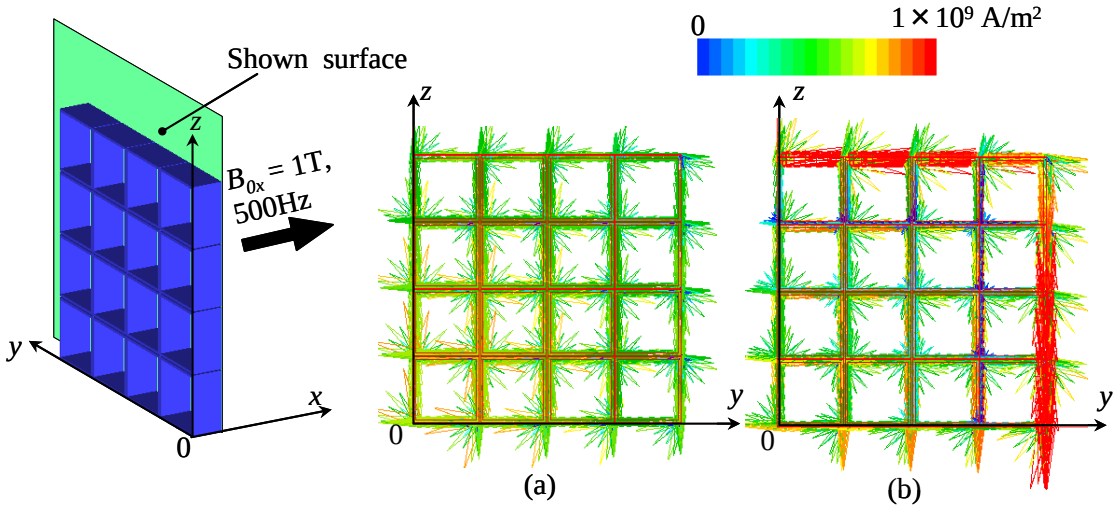

Fig.4. 3. Eddy current distribution of the real model with gaps at x=50 at instant when applied field is (a) maximum and (b) zero (G = 2, L = 50, f = 500Hz).

4.3.3 Determination of effective permeability of magnetic body

For example, the x-component μ_{hx}* of μ_h* of magnetic body suitable for the real model with gaps can be determined as follows. The linear ac steady-state eddy current analysis of the cell model in the uniform ac flux density B_{0x}, shown in Fig. 4.4, is carried out by using (4-1) and (4-2). The cell model is one square cylinder surrounded by air with thickness of 1 mm. The obtained magnetic field $H_{air,x}$* in the air surrounding the cylinder is the generated magnetic field intensity without the compensation magnetic field due to the eddy currents [7]. Therefore, μ_{hx}* can be determined by using the following equation:

$$\mu_{hx}^{*} = B_{0x} \Big/ H_{air,x}^{*} , \tag{4-5}$$

$$H_{air,x}^{*} = \sum_{ie=1}^{N_{air}} H_{x}^{*(ie)} \cdot V^{(ie)} \Big/ \sum_{ie=1}^{N_{air}} V^{(ie)} , \tag{4-6}$$

where V is the volume of each element ie and N_{air} is the total element number of

the air region. The other components can be obtained in the same way and μ_h* becomes anisotropic.

4.3.4 Results and Discussion

The anisotropic relative permeability μ_{hr}* determined by using the method mentioned in section IV. *B* is μ_{hrx}* = 0.11-0.13*i*, μ_{hry}*=μ_{hrz}*= 0.11-0.12*i*. These values are almost the same with the isotropic μ_{hpr}* in Fig. 4.2.

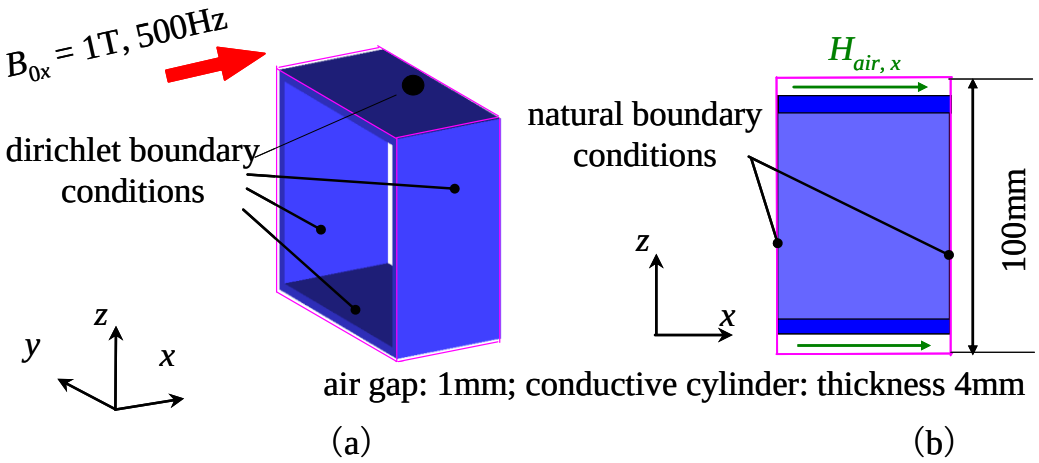

Fig. 4.4. Cell model for homogenization technique with magnetic body with effective permeability. (a) bird's eye view, (b) cross section at *x*-*z* plane.

The flux distribution $|B|_{p\text{-}q}$ obtained from the homogeneous magnetic body of μ_h* are almost the same with that of μ_{hp}* shown in Fig. 4.2. The contour maps of the maximum flux densities at *x* = 60 and 150 mm obtained from the real model and the magnetic body with μ_h* and its error distributions are shown in Fig. 4.5and Fig.4. 6, respectively.

The magnetic body cannot represent the detailed flux distribution at *x* = 60 near

the shielding wall, whereas the flux distributions at x = 150 obtained using the real model and magnetic body are in good agreement with each other.

As we can see from Fig.4. 6, the error distributions of the flux density x = 150 are within 2%, whereas the error distributions at x = 60 are very large because the reason mentioned before.

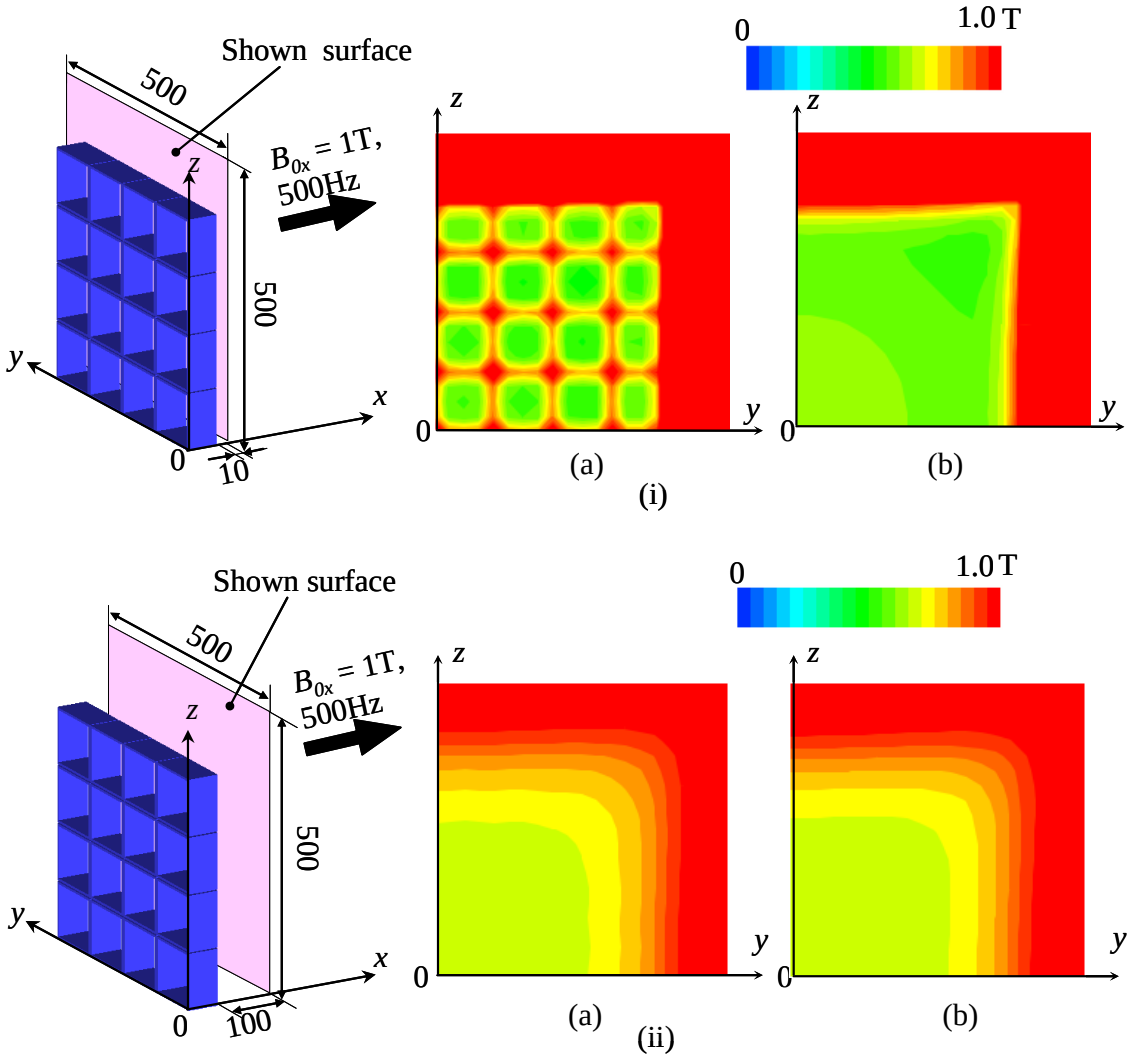

Fig. 4.5. Contour maps of the maximum absolute flux densities obtained from (a) real model with gaps, (b) homogenization magnetic body at (i) x = 60 and (ii) x = 150 (G = 2, L = 50, f = 500Hz).

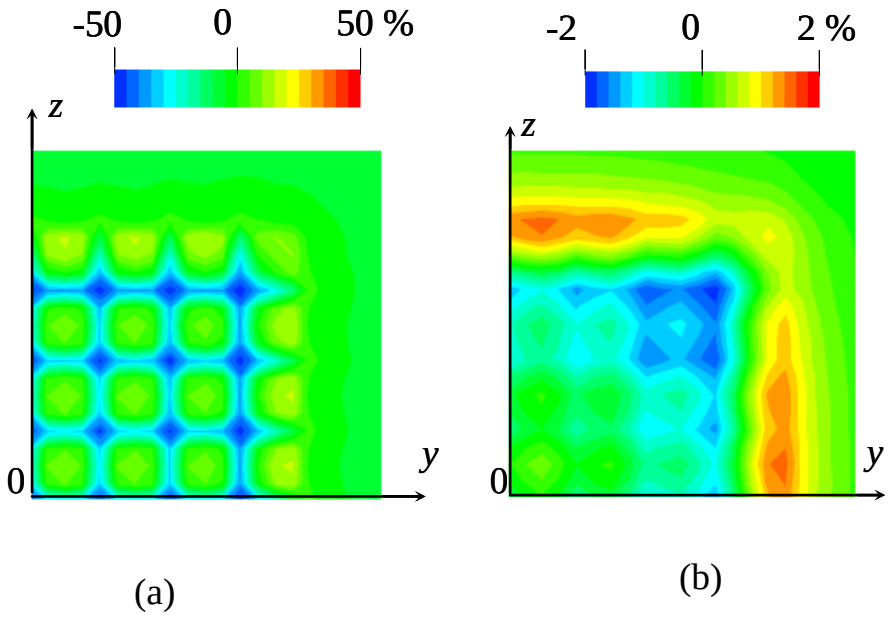

(a) (b)

Fig. 4.6. Contour maps of error distribution of the maximum absolute flux densities at (a) x = 60 (b) x = 150 (G = 2, L = 50, f = 500Hz).

Table 4.1 shows the discretization data and CPU time of the real model with gaps and its homogenization model. As we can see from the table. If the same mesh was used in the homogenization model. The CPU time of the homogenization technique is less compared with the real model analysis. Meanwhile, if the coarse mesh was used in the homogenization technique, the CPU time is much smaller. What is more, the memory requirements is also smaller.

Table 4.1 Discretization Data and CPU time of the real model with gaps and its homogenization model

Model	real	homogenization	
Mesh	fine		coarse
Number of elements	90,593		8,228
Number of nodes	98,568		9,522
Number of edges	287,564		27,209
Number of unknowns	294,240	277,345	24,129
Number of non-zeros	5,537,693	4,514,042	379,421
Memory requirements (MB)	313	269	37
Number of iterations of ICCG method*	1,569	380	164
Total CPU time (s)	1588	166	18

Computer used : Intel Core i7 2.7GHz
Convergence criterion for ICCG method : 10^{-7}

4.4 Verification for Homogenization of Real Model Without Gaps

4.4.1 Model description

In the real model without gaps, length *L*, width *W*, and thickness *t* of the cylinders are 10, 100, and 4 mm, respectively, and the frequency *f* of the magnetic field is chosen as 50 Hz. The conductivity σ and relative permeability μ_s of the cylinders are 2×107 S/m and 1, respectively.

4.4.2 Selection of suitable technique

First, the suitable homogenization technique for the real model without gaps is

examined by using the same procedure as in section 4.4.2. The flux distributions $|B|_{p\text{-}q}$'s obtained using the real model without gaps and its homogeneous magnetic and conductive bodies are shown in Fig. 4.7. This figure shows that the conductive body should be used contrary to the model with gaps because the homogeneous conductive body can represent the eddy current paths of the real model without gaps shown in Fig. 4.8.

4.4.3 Determination of effective conductivity of conductive body

Two methods for determining the modified conductivity σ_h of the conductive body suitable for the real model without gaps are investigated in this paper.

First, the modified conductivity σ_{hv} is determined by the ratio of the volume V_r of the conductor in the real model to the volume V_h of the homogeneous conductive body as follows:

$$\sigma_{hv} = \sigma \cdot V_r / V_h \ , \tag{4-7}$$

Second, the modified conductivity σ_{hr} is determined by equating the resistance R_h of the homogenization cell model with the resistance R_r of the real cell model in each direction. For example, the resistance R_{rz} of the real cell model in z direction can be obtained by the current analysis with the finite element method when the voltage is applied in z direction as shown in Fig. 4.9(a). R_{hz} with σ_{hr} can be easily obtained because the current is uniform in the homogeneous conductive body as shown in Fig. 4.9(b). The other components can be obtained in the same way, and σ_{hr} becomes anisotropic.

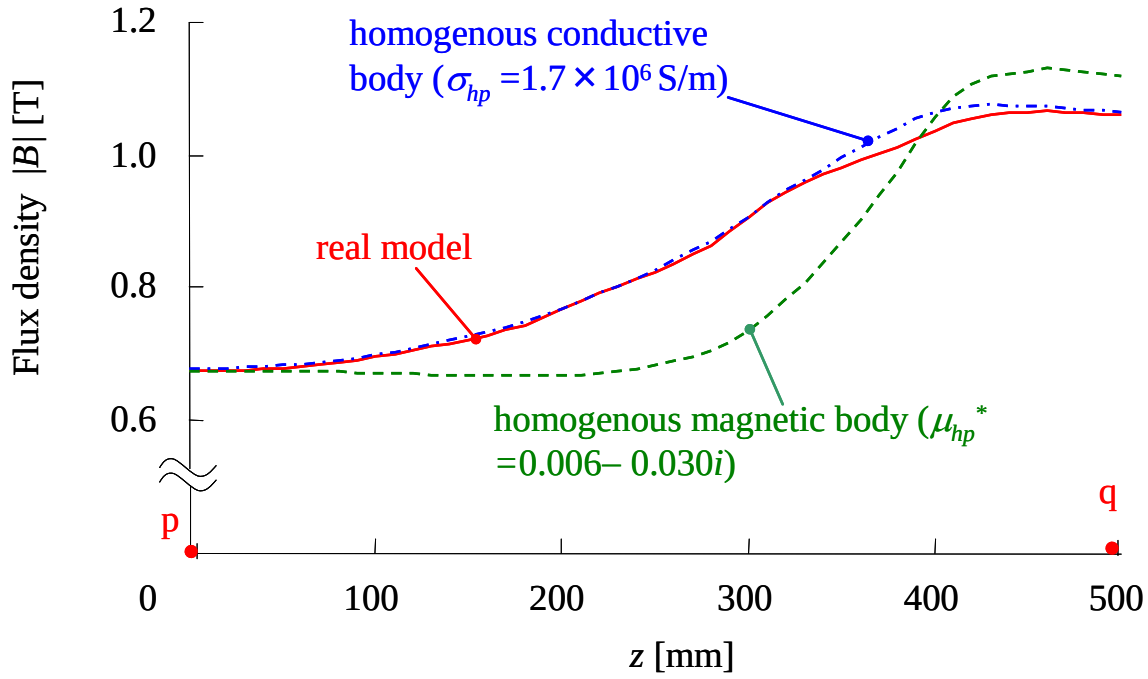

Fig. 4.7. Flux distribution on line p-q obtained using the real model without gaps and its homogeneous bodies (G=0, L=10, f=50Hz).

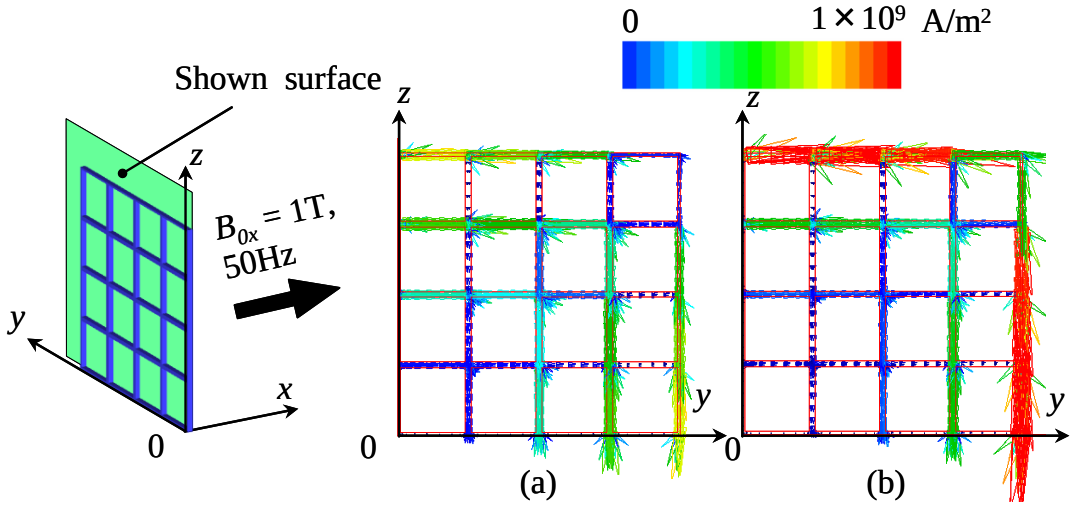

Fig. 4.8. Eddy current distribution of the real model without gaps at x=10 at instant when applied field is (a) maximum and (b) zero (G=0, L=10, f=50Hz).

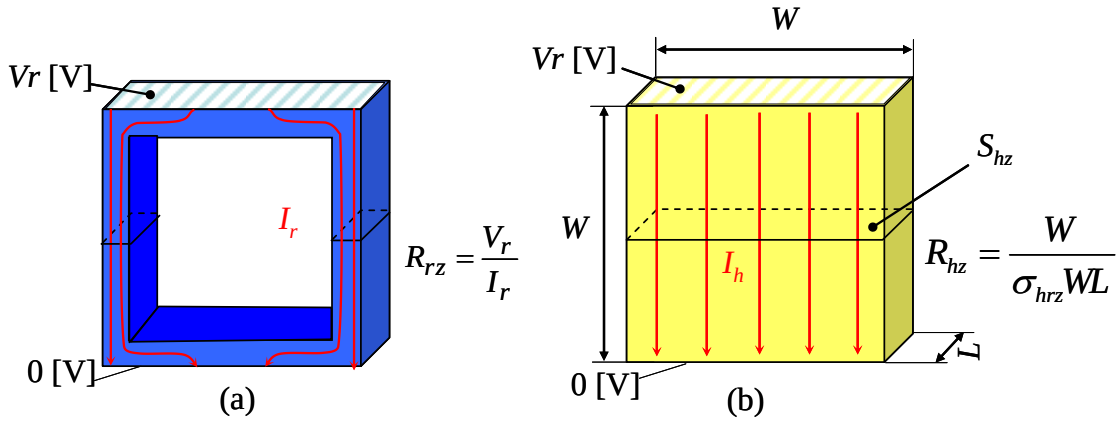

Fig. 4.9. Current distribution in (a) real model, (b) homogeneous conductive body when the voltage is applied in the z-direction.

4.4.4 Results and Discussion

The modified conductivity σ_{hv} determined by the volume ratio is 3.07×10^6 S/m. The anisotropic modified conductivity σ_{hr} determined by the resistance in each direction is σ_{hrx} =3.07×10^6 S/m, σ_{hry}=σ_{hrz}= 1.64×10^6 S/m. The values of σ_{hry} and σ_{hrz}, which greatly affect the eddy currents, are almost the same with the isotropic σ_{hp} in Fig. 4.7.

The flux distributions $|B|_{p\text{-}q}$'s obtained using the real model without gaps and its homogeneous conductive bodies with σ_{hv} and σ_{hr} are compared in Fig.4.10. It shows that the conductive body with σ_{hr} determined by the resistance in each direction should be used because the eddy currents in the real model without gaps almost flow in equidistant conductive frames only as shown in Fig.4.7. The contour maps of the maximum flux densities at x = 20 and 100 mm obtained from the real model and the

conductive body with the anisotropic σ_{hr} and its error distributions are shown in Fig.4.11 and Fig.4.12, respectively. As the same with the model with gaps, the homogeneous conductive body cannot represent the detailed flux distribution near the shielding wall, whereas the flux distribution at x = 100 mm obtained using the real model and the conductive body are in good agreement with each other. As it was shown in Fig.4. 12, the errors are within 3% when the surface is at x = 100 mm, whereas the error distributions at x = 60 are very large.

The eddy current distribution obtained from the conductive body with σ_{hr} is shown in Fig. 4.13. The values of eddy currents obtained from the conductive body are much different from those obtained from the real model without gaps shown in Fig.4. 8 due to homogenization, whereas the tendencies are in good agreement with each other.

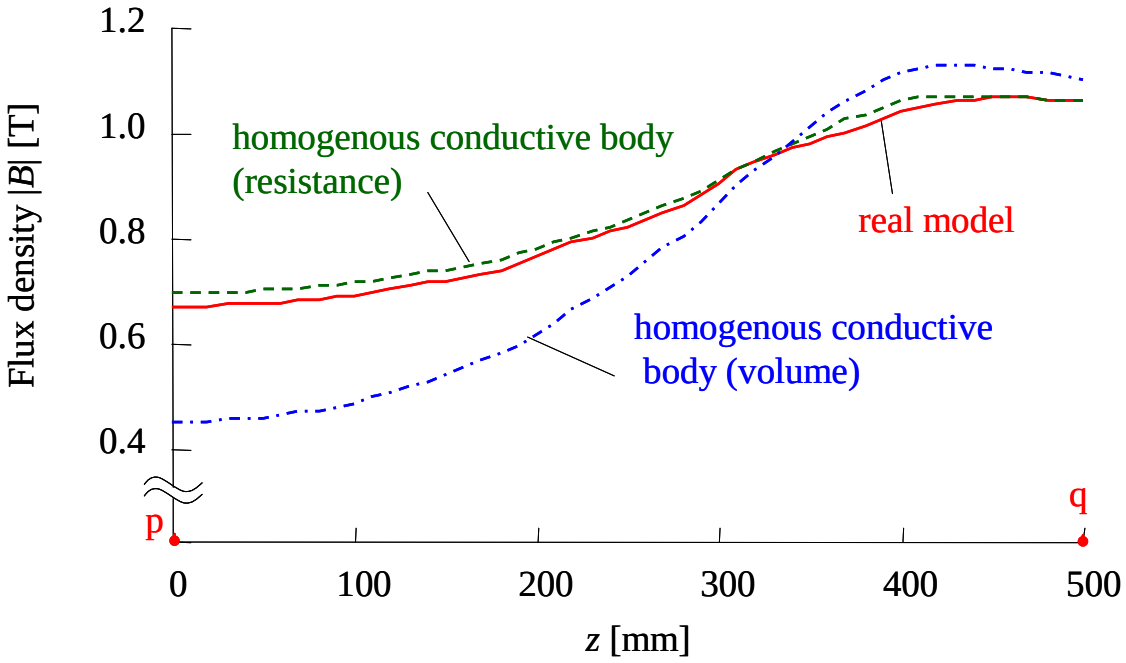

Fig.4. 10. Flux distribution on line p-q obtained from the real model without gaps and conductive bodies (G=0, L=10, f=50Hz).

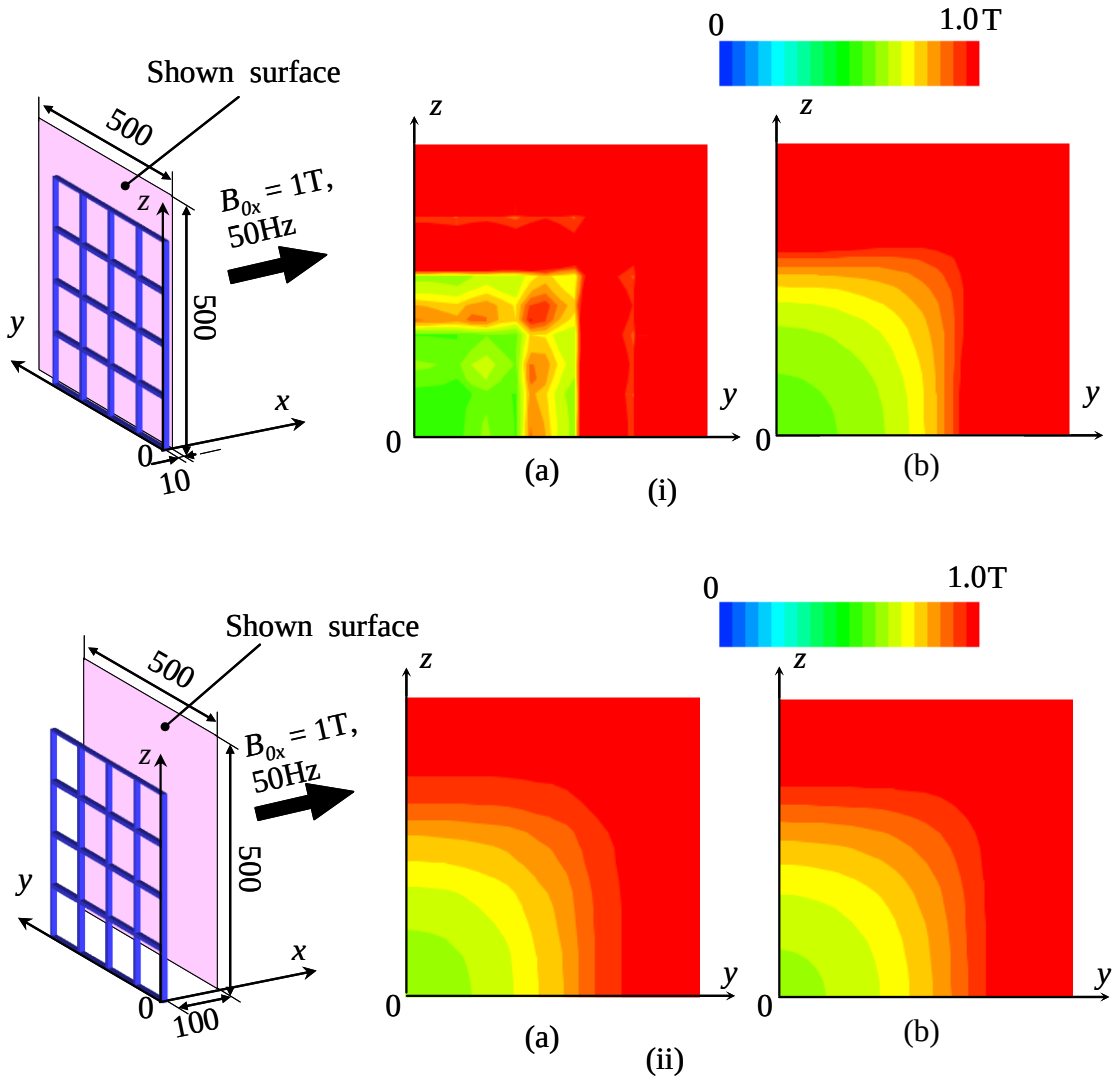

Fig. 4.11. Contour maps of the maximum absolute flux densities obtained from (a) real model without gaps, (b) homogeneous conductive body at (i) x =20 and (ii) x = 100 (G=0, L=10, f=50Hz).

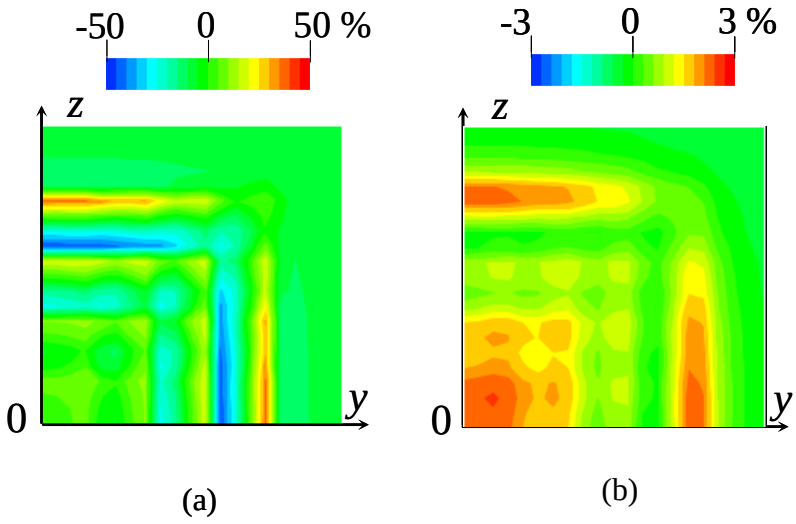

Fig. 4.12. Contour maps of error distribution of the maximum absolute flux densities at (a) x = 20 (b) x = 100 (G = 2, L = 50, f = 500Hz).

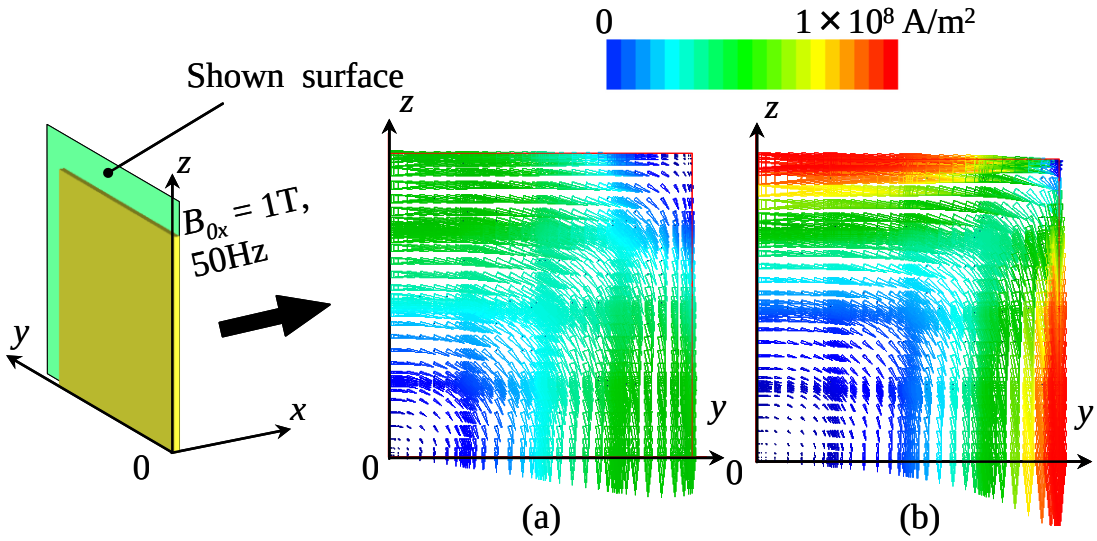

Fig.4.13. Eddy current distribution of the conductive body at x=10 at instant when applied field is (a) maximum and (b) zero (G=0, L=10, f=50Hz).

Table 4.2 shows the discretization data and CPU time of the real model without gaps and its homogenization model. As we can see from the table. If the same meshes was used in the homogenization model. The CPU time of the homogenization technique is more compared with the real model analysis. But if the coarse mesh was used in the homogenization technique, the CPU time is much smaller. Meanwhile, the memory requirements is also smaller.

Table 4.2 Discretization Data and CPU time of the real model without gaps and its homogenization model

Model	real	homogenization	
Mesh	fine		coarse
Number of elements	47,040		7,260
Number of nodes	51,984		8,464
Number of edges	150,879		24,127
Number of unknowns	150,015	153,151	22,183
Number of non-zeros	2,677,982	2,874,110	380,618
Memory requirements (MB)	160	190	37
Number of iterations of ICCG method*	1,135	1,636	1,280
Total CPU time (s)	343	523	108

Computer used : Intel Core i7 2.7GHz
Convergence criterion for ICCG method : 10^{-7}

4.5 Summary

In this section, it is shown that accurate homogenization analyses of the models

composed of periodic conductive and non-magnetic components are possible using the suitable techniques. The magnetic body with the effective anisotropic complex permeability μ_h* is suitable for the real model in which each component is insulated. On the other hand, the conductive body with the modified anisotropic conductivity σ_{hr} determined by the resistance is suitable for the real model, in which each component is connected.

In the homogenization technique of model composed of distributed component, that accurate homogenization analyses of the models composed of periodic conductive and non-magnetic components are possible using the suitable techniques. What is more, the conductive body with the modified anisotropic conductivity σ_{hr} determined by the resistance is suitable for the real model, in which each component is connected.

Chapter 5 Conclusion and Recommendation

In this thesis, to apply the homogenization technique of laminated cores taking account of eddy currents in the steel plates to motor cores, the 3D sub-analysis model of steel plate is proposed. The accuracy is much improved by the 3D sub-analysis compared with the ordinary 1D sub-analysis. However, the error due to the edge effect of the cores occurs because the steel plate is assumed to be infinite in the proposed 3D sub-analysis.

Then, in the homogenization technique of the model composed of distributed components, it is shown that accurate homogenization analyses of the models composed of periodic conductive and non-magnetic components are possible using the suitable techniques. The magnetic body with the effective anisotropic complex permeability μ_h* is suitable for the real model in which each component is insulated. On the other hand, the conductive body with the modified anisotropic conductivities σ_{hr} determined by the resistance is suitable for the real model, in which each component is connected.

In Chapter 1, the research background of this thesis is presented with an important viewpoint that the homogeneous techniques is important for modeling of laminated core and models composed of distributed components.

Chapter 2 expresses the method of 3D eddy current analysis. First, the fundamental equations are introduced. Then, the discretization is carried out by FEM.

Chapter 3 expresses the homogenization technique of the laminated core under

rotational flux. And the verifications for these proposed modeling methods are presented. As it is shown in this chapter, the proposed method is much better to calculate the eddy current losses when the laminated core is under rotational flux compared with the one-dimensional method.

Chapter 4 expresses the homogenization technique of the model composed of distributed components.The real model with and without gaps are included. Finally, the verification of the method is presented. It is shown that accurate homogenization analyses of the models composed of periodic conductive and non-magnetic components are possible using the suitable techniques. The magnetic body with the effective anisotropic complex permeability μ_h* is suitable for the real model in which each component is insulated. On the other hand, the conductive body with the modified anisotropic conductivity σ_{hr} determined by the resistance is suitable for the real model, in which each component is connected.

In the future ,as to the modeling of laminated core, the 3D sub-analysis model taking account of the nonlinearity and the edge effect of steel plate will be developed and applied to an actual motor.

In the homogenization technique of the model composed of distributed component, that accurate homogenization analyses of the models composed of periodic conductive and non-magnetic components are possible using the suitable techniques. What is more, the conductive body with the modified anisotropic conductivity σ_{hr} determined by the resistance is suitable for the real model, in which each component is connected.

In the future, the homogenization techniques proposed will be applied for

different models and expanded for conductive and magnetic components such as soft magnetic composite materials, etc.

References

[1] Y. Takahashi, S. Wakao, K. Fujiwara, S. Fujino, "Large-Scale Magnetic Field Analysis of Laminated Core by Using the Hybrid Finite Element and Boundary Element Method Combined with the Fast Multipole Method," *IEEE Transactions on Magnetics*, vol. 43, no. 6,pp.2971-2973, 2007.

[2] K. Yamazaki, K. Kato, K. Ono, H. Saegusa, K. Tokunaga, Y. Iida, S. Yamamoto, K. Ashiho, K. Fujiwara, N. Takahashi, "Analysis of Magnetic Disturbance Due to Buildings," *IEEE Transactions on Magnetics*, vol. 39, no. 5, pp. 3226-3228, 2003.

[3] K. Yamazaki, K. Kato, K. Muramatsu, K. M. Uchida, K. Fujiwara, M. Miyamoto, H. Kaneko, H. Saegusa, "A practical Method for Evaluating Magnetic Disturbance Due to Buildings for The Design of A Magnetic Testing Site," *IEEE Transactions on Magnetics*, vol. 41, no. 5, pp. 1856-1859, 2005.

[4] K. Yamazaki, S. Hirosato, K. Kamata, K. Muramatsu, K. Kobayashi, A. Haga, "Open-Type Magnetically Shielded Room Combined With Square Cylinders Made of Magnetic and Conductive Materials for MRIs," *IEEE Transactions on Magnetics*, vol. 44, no. 11 pp. 4183-4186, 2008.

[5] L. Krahenbuhl and D. Muller, "Thin Layers in Electrical Engineering. Example of Shell Models in Analyzing Eddy Currents by Boundary and Finite Element Method," *IEEE Transactions on Magnetics*, vol. 29, pp. 1450–1455, Mar.1993.

[6] H. Igarashi, A. Kost, and T. Honma, "A Three Dimensional Analysis on Magnetic Field Around A Thin Magnetic Conductive Layer Using Vector

Potential," *IEEE Transactions on Magnetics*, vol. 34, pp. 2539–2542, Sept. 1998.

[7] P. Dular, J. Gyselinck, C. Geuzaine, N. Sadowski, and J. P. A. Bastos, "A 3-D Magnetic Vector Potential Formulation Taking Eddy Currents in Lamination Stacks Into Account," *IEEE Transactions on Magnetics*, vol. 39, pp. 1147–1150, 2003.

[8] K. Muramatsu, T. Okitsu, H. Fujitsu, and F. Shimanoe, "Method Of Nonlinear Magnetic Field Analysis Taking Into Account Eddy Current in Laminated Core," *IEEE Transactions on Magnetics*, vol. 40, no. 2, pp. 896–899, 2004.

[9] Y. Gao, K. Muramatsu, K. Shida, K. Fujiwara, S. Fukuchi, and T. Takahata, "Loss Calculation of Reactor Connected to Inverter Power Supply Taking Account of Eddy Currents In Laminated Steel Core," *IEEE Transactions on Magnetics*, vol. 45, no. 3, pp. 1044–1047, 2009.

[10] T. Matsuo, Y. Terada, M. Shimasaki, "Representation of AC Hysteretic Characteristics of Silicon Steel Sheet Using Simple Excess Eddy-current Loss Approximation," *IEEE Transactions on Magnetics*, vol. 41, no. 5, pp. 1544-1547, 2005.

[11] H. Kaimori, A. Kameari, K. Fujiwara, "FEM Computation of Magnetic Field and Iron Loss in Laminated Iron Core Using Homogenization Method," *IEEE Transactions on Magnetics*, vol. 43, no. 4, pp. 1405-1408, 2007.

[12] G. Grandi, M.K. Kazimierczuk, A. Massarini, U. Reggiani, G. Sancineto, "Model of Laminated Iron-Core Inductors for High Frequencies," *IEEE Transactions on Magnetics*, vol. 40, no. 4, pp. 1839-1845, 2004.

[13] H. Igarashi, K. Watanabe, A. Kost, “A Reduced Model for Finite Element Analysis of Steel Laminations,” *IEEE Transactions on Magnetics*, vol. 42, no. 4, pp. 739-742, 2006.

[14] J. Gyselinck, R.V. Sabariego, P. Dular, “A Nonlinear Time-Domain Homogenization Technique for Laminated Iron Cores in Three-Dimensional Finite-Element Models,” *IEEE Transactions on Magnetics*, vol. 42, no. 4, pp.763-766, 2006.

[15] J. Pippuri, A. Arkkio, “Time-Harmonic Induction-Machine Model Including Hysteresis and Eddy Currents in Steel Laminations,” *IEEE Transactions on Magnetics*, vol. 45, no. 7, pp. 981-2989, 2009.

[16] J. C. M. Garnett, “Colors in Material Glasses and Metal Films,” *Trans. Roy. Soc.*, vol. 53, pp. 385–420, 1904.

[17] B. Sareni, L. Krahenbuhl, A. Beroual, A. Nicolas, and C. Brosseau, “A Boundary Integral Equation Method For The Calculation of The Effective Permittivity of Periodic composites,” *IEEE Transactions on Magnetics*, vol. 33, no.2, pp. 1580–1583, 1997.

[18] O. Bottauscio, V. C. Piat, M. Chiampi, M. Codegone, and A. Manzin, “Nonlinear Homogenization Technique for Saturable Soft Magnetic Composites,” *IEEE Transactions on Magnetics*, vol. 44, no. 11, pp. 2955–2958, 2008.

[19] H. Waki, H. Igarashi, and T. Honma, “Analysis of Magnetic Shielding Effect of Layered Shields Based on Homogenization,” *IEEE Transactions on Magnetics*, vol. 42, no. 4, pp. 847–850, 2006.

[20] S. Odawara, Y. Haraguchi, K. Muramatsu, K. Yamazaki, and S. Hirosato, "Magnetic Field Analyses of Architectural Components Using Homogenization Technique," *IEEE Transactions on Magnetics*, vol. 46, no. 8, pp. 3313–3316, 2010.

[21] S. Hirosato, K. Yamazaki, Y. Haraguchi, Y. Gao, K. Muramatsu, A. Haga, K. Kamata, H. Sasaki, K. Kobayashi, "Design Method for Realization of Open-Type Magnetically Shielded Room Composed of Magnetic Square Cylinders for MRI," *IEEE Transactions on Magnetics*, vol. 47, no. 5, pp. 954 - 957, 2011.

[22] J. Pedro, A. Bastos and N. Sadowski, "Electromagnetic Modelling By Finite Element Methods", Marcel Dekker, INC, 2003.

[23] Bhag Singh Gur and Huseiyin R. Hizirogulu, "Electromagnetic Field Theory Fundamentals", China machine press, 2002.

[24] S. J. Salon, "Finite Element Analysis of Electrical Machines", Kluwer Academic Publishers, 1995.

[25] M. L. Barton and Z. J. Cendes, "New Vector Finite Elements for Three-Dimensional Magnetic Field Computation," *J. Appl. Phys.*, vol. 61, no. 8, pp. 3919-3921, 1987.

[26] A. Bossavit, "A Rotational for Edge-Element in 3D Fields Computations," *IEEE Transactions on Magnetics*, vol. 24, pp. 74-79, 1988.

[27] Z. J. Cendes, "Vector Finite Element for Electromagnetic Field," *IEEE Transactions on Magnetics*, vol. 27, no. 9, pp. 3958-3966, 1991.

[28] A. Kameari, "Calculation of Transient 3D Eddy Current Using Edge Elements,"

IEEE Transactions on Magnetics, vol. 26, no. 3, pp. 466-469, 1990.

[29] D. R. Tanner and A. F. Peterson, "Vector Expansion Functions for the Numerical Solution of Maxwell's Equations, Micorwave," *Opt. Tech. Lett.*, vol. 2, no. 2, pp. 331-334, 1989.

[30] J. F. Lee, D. K. Sun, and Z. J. Cendes, "Tangential Vector Finite Elements for Electromagnetic Field Computation," *IEEE Transactions on Magnetics*, vol. 27, no. 9, pp. 4032-4035, 1991.

[31] K. Yamazaki, "An Efficient Procedure to Calculate Equivalent Circuit Parameter of Induction Motor Using 3-D Nonlinear Time-Stepping Finite–Element Method", *IEEE Transactions on Magnetics*, vol. 38, no. 2, pp. 1281-1284, 2002.

[32] K. Yamazaki, N. Fukushima, "Torque and Loss Calculation of Rotating Machines Considering Laminated Cores Using Post 1-D Analysis," *IEEE Transactions on Magnetics*, vol. 47, no. 5, pp. 994-997, 2011.

[33] H. Gersem, S. Vanaverbeke, G. Samaey, "Three-Dimensional–Two-Dimensional Coupled Model for Eddy Currents in Laminated Iron Cores," *IEEE Transactions on Magnetics*, vol. 48, no. 2, pp.815-818, 2012.

Publications

A. Journal Paper

A-1 Lin Cheng, S. Sudo, Y. Gao, H. Dozono, K. Muramatsu, “Homogenization Technique of Laminated Core Taking Account of Eddy Currents Under Rotational Flux Without Edge Effect,” ***IEEE Transactions on Magnetics***, vol. 49, no. 5, pp. 1969-1972, 2013.

B. International Conferences

B-1 Lin Cheng, S. Sudo, Y. Gao, H. Dozono, K. Muramatsu, “Homogenization Technique of Laminated Core Taking Account of Eddy Currents in Steel Plates Under Rotational Flux,” ***The 15th Biennial IEEE Conference on Electromagnetic Field Computation***, no. WP2-23, Oita, 2012.11.

B-2 Lin Cheng, K. Ikenaga, Y. Gao, H. Dozono, K. Muramatsu, “Homogenization Techniques of Conductive and Non-Magnetic Components Taking Account of Eddy Currents in Magnetic Field Analysis,” ***The 19th Conference on the Computation of Electromagnetic Fields***, no. PB5-18, Budapest, Hungary, 2013.7.